SIAM J. APPL. MATH.
Vol. 70, No. 2, pp. 369–409

PEM FUEL CELLS: A MATHEMATICAL OVERVIEW*

KEITH PROMISLOW† AND BRIAN WETTON‡

Abstract. We present an overview of the mathematical issues that arise in the modeling of polymer electrolyte membrane fuel cells. These issues range from nanoscale modeling of network structures arising in pore formation within the polymer and the formation of nanostructured agglomerates within the catalyst layer, to macroscale models of multiphase flow and water management, degradation of catalyst layers and membrane, and development of stack level codes. The dominant themes are the development and analysis of multiscale models and their reduction to simplified forms that are implementable in stack-level computations.

Key words. polymer electrolyte membrane fuel cell, multiscale models, functionalized Lagrangians, nanostructured networks

AMS subject classifications. 35M10, 41A60, 49S05, 65M06, 74F10, 76T30

DOI. 10.1137/080720802

1. Introduction.

The broad spectrum of energy use—its generation, transportation, and conversion—is emerging as one of the most important political and social issues of the 21st century. Our current energy infrastructure relies heavily upon the availability of cheap, high energy density fuels extracted from fossil reserves that are either refined and shipped or combusted to produce electricity. Concerns about dwindling resources, particularly as measured against consumption, and the accumulating impact of carbon dioxide on the global environment are uniting to push interest in a sustainable, carbon-lite energy infrastructure. This requires the accumulation of energy from ambient sources (wind, solar, geothermal) and its subsequent conversion, into either high-density forms or electricity, for distribution. But electric power, which can be efficiently distributed, is problematic to store on a large scale and must be converted to a high-density state for automotive uses. Thus a key issue in the transition away from a carbon-based energy infrastructure is the efficient conversion of energy from solar, chemical, and thermal to electric, or from electric or solar to chemical.

Fuel cells are highly efficient electrochemical (chemical to electric) energy conversion devices. On a macroscale the chemical fuel and oxygen are fed into two electrodes, the anode and cathode, that are separated by a selective transport membrane. The catalyst materials within each electrode induce a partial reaction that produces electrons at the anode and consumes electrons at the cathode. The partial reactions also produce ions, and the net reaction is completed by transporting one of the charged ions through the selective transport membrane that ideally blocks transport of the other species—particularly the electrons that flow through an external circuit from anode to cathode. Separating the reaction into two half-steps occurring at different electrodes stores the Gibbs free energy of the chemical reaction, i.e., the full energy less entropic losses, in charged double layers at the surface of the respective catalyst

*Received by the editors April 9, 2008; accepted for publication (in revised form) September 22, 2008; published electronically July 17, 2009.
http://www.siam.org/journals/siap/70-2/72080.html
†Department of Mathematics, Michigan State University, East Lansing, MI 48824 (kpromisl@math.msu.edu). This author's work was supported by NSF grants DMS 0405965 and DMS 0708804.
‡Department of Mathematics, University of British Columbia, Vancouver, V6T 1Z2 BC, Canada (wetton@math.ubc.ca). This author's work was funded by an NSERC Canada grant.

layers. When the chemical reaction is completed in a single step, the excess energy becomes heat; when separated into two steps, a significant portion of the chemical potential is available to the cell as a difference in electric potential.

Polymer electrolyte membrane (PEM) fuel cells employ a hydrophobic polymer, functionalized by acidic sidechains, as the electrode separator. They enjoy rapid start-up and shut-down transients and efficient operation when hydrogen gas is used as the fuel. Moreover, they possess a very rich, multiscale structure that requires many levels of models to describe. Indeed, an emerging theme in the realm of energy conversion is the need for nanostructured composites composed of interpercolating networks with selective transport properties feeding reactants to catalyst sites with large surface area densities. We focus our attention on the mathematical description of their operation with attention towards the optimization of performance. This includes the development of structured nanocomposites, such as the catalyst layers and electrode separator; the understanding of the macroscopic properties that influence the fuel cell performance under different operating conditions, such as the multiphase flow associated with water management; the modeling of various parasitic reactions that can degrade the fuel cell's performance over time, particularly corrosion of carbon in the catalyst layer; and finally the integration of subscale models into stack-level codes that describe the operation of hundreds of fuel cells in series.

2. Basic PEM fuel cell functionality. A PEM fuel cell is divided into an anode and a cathode, separated by the PEM. The cathode has a graphite current collector plate into which are etched gas flow channels that carry an oxygen, nitrogen, and water vapor mixture. The collector plate also contains coolant channels that remove heat generated by the reaction. The gases permeate the gas diffusion layer (GDL) that carries the oxygen to the cathode catalyst layer. Similarly, on the anode the fuel, a mixture of molecular hydrogen, water vapor, and other inert gases, flows down the channels etched into the anode collector plate; see Figure 2.1 (top). The full mixture reaction,

$$2H_2 + O_2 \to 2H_2O, \tag{2.1}$$

is split into the anode and cathode half-reactions, respectively, the hydrogen oxidation (HO) and the oxygen reduction reaction (ORR),

$$H_2 \to 2H^+ + 2e^-, \tag{2.2}$$

$$4H_3O^+ + 4e^- + O_2 \to 6H_2O. \tag{2.3}$$

There are detailed studies of these reactions [62] and their thermodynamics [54] under idealized conditions. However, reaction rates and heat production depend sensitively upon local conditions, and in practice macroscopic models, such as the Butler–Volmer equations (2.5)–(2.6), are fit to the performance of specific catalyst layer construction. Both the anode and cathode catalyst layers are interpenetrating nanocomposites of electronically conductive carbon, protonically conductive ionomer, and gas pore space. The 20–40 nanometer carbon black particles are decorated with 5 nanometer platinum (Pt) catalyst particles and mixed with the ionomer and alcohol. This catalyst "ink" is applied to either side of the polymer electrolyte membrane. As the mixture dries the carbon particles agglomerate into 100–200 nanometer diameter clusters that are coated in polymer electrolyte. As the last of the alcohol dries off, the mixture cracks slightly, forming a network of gas pores; see Figure 2.1 (bottom). The protons formed

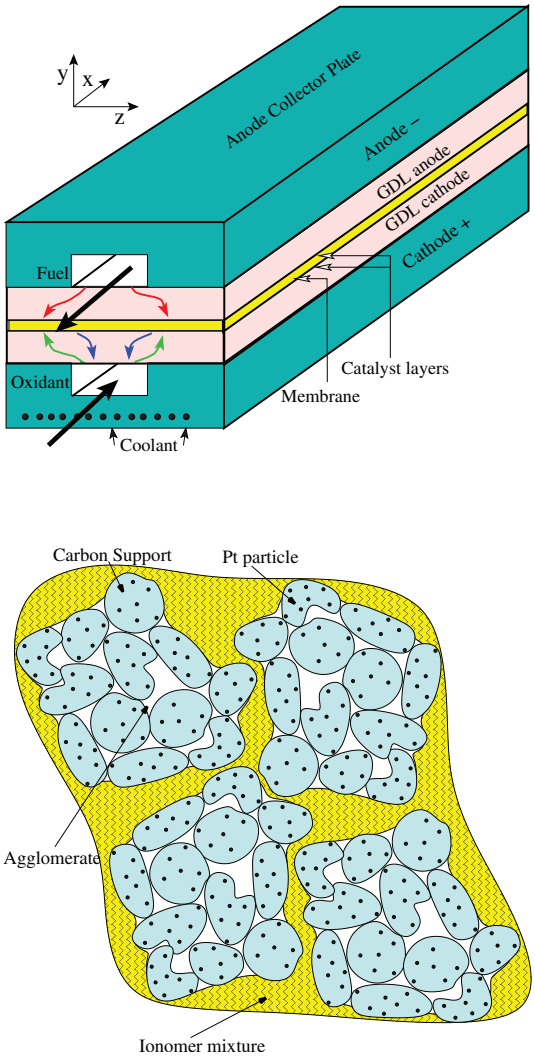

FIG. 2.1. *Top: Three-dimensional (3D) schematic of unit cell, not to scale. A single fuel (hydrogen) channel and an oxidant (air) channel are shown, although a unit cell typically has many. The gas diffusion layers, catalyst layers, and polymer electrolyte membrane comprise the MEA, which is sandwiched between the anode and cathode collector plates. Oxygen (green) flows through the cathode GDL to the catalyst layer while product water (blue) flows in the reverse direction. Bottom: The catalyst layer is a nanocomposite of carbon particles decorated with platinum and an interpercolating region of ionomer material (denatured polymer electrolyte, a protonic conductor).*

by HO at the anode are driven across the water-filled pores of the polymer electrolyte membrane by the induced voltage gradient, arriving in the cathode catalyst as hydronium ions, H_3O^+. The electrons in the anode catalyst layer are conducted through its carbon agglomerates, through the graphite paper of the GDL, and into the graphite backing plate, around an external circuit, and into the cathode graphite plate, the cathode GDL, ultimately arriving at the carbon agglomerates within the cathode catalyst layer. At the surface of the platinum catalyst within the cathode catalyst layer, the electrons combine with the protons transported through the ionomer phase and

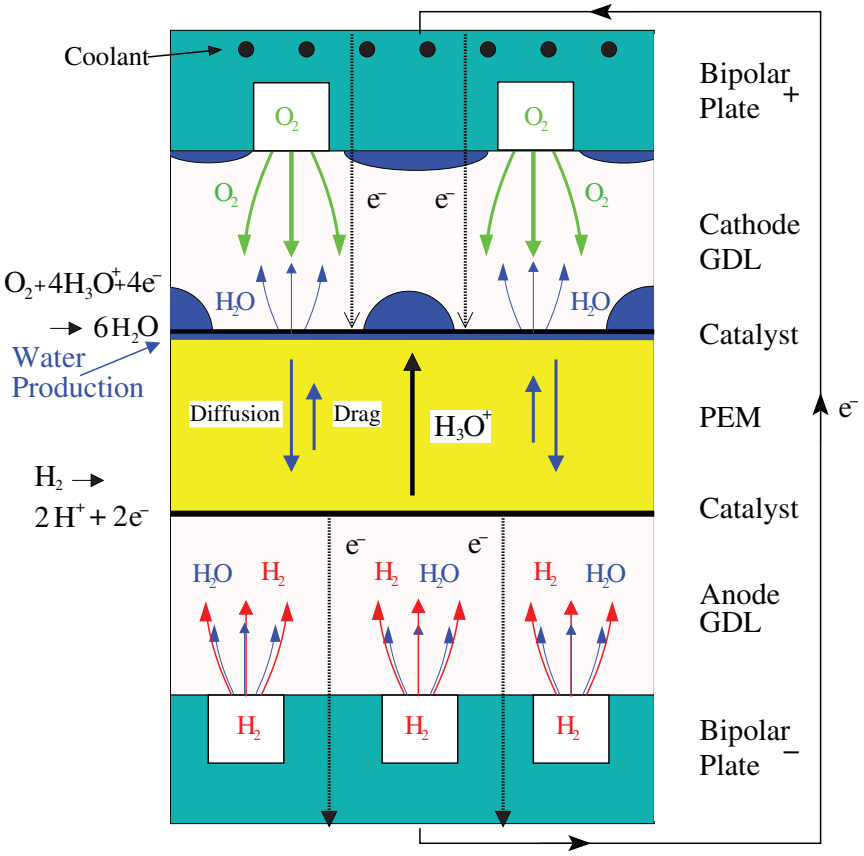

FIG. 2.2. *Cross-section of a unit cell in the y-z plane (not to scale). Water is formed at the cathode catalyst, which may occur in liquid or vapor form. Liquid water hydrates the membrane and increases its protonic conductivity, but may also flood the catalyst layer pores, preventing oxygen from reaching the catalyst layers.*

the molecular oxygen that has diffused through the GDL, into the cathode catalyst, through its gas pore structure, and into the carbon agglomerates.

The schematic of a unit cell in Figure 2.1 (top) depicts counterflow in which the oxidant gas (air) and coolant flow in channels in the x direction while the reactant gas (hydrogen) flows in channels in the $-x$ direction. Under coflow operation both gas channels flow in the $+x$ direction. The straight gas channels depicted in this figure are typical of the Ballard Mk 9 design; however, serpentine gas channels [100] are also used. While the serpentine gas channels increase the overall channel length and so the parasitic losses to gas compressors, the increased pressure drop can be useful for removal of liquid water which may accumulate in the channels. Unit cells can be of the order of a meter long, but only a few millimeters thick. Reductions to unit cell and stack models based on this large aspect ratio are discussed in section 6.

More detail of the cross-plane (y-z) geometry is shown in Figure 2.2. Hydrogen gas moves from channels through the anode GDL, often composed of a teflonated carbon fiber paper, to the catalyst layer. The carbon fibers are good conductors of heat and electronic current. The GDL thickness is of the order of 100 micrometers, while the catalyst layer is of the order of 10 micrometers thick. The two pairs of GDL

and catalyst layers together with the membrane are called the membrane electrode assembly (MEA). Designing improved MEAs is the goal of much current industrial and academic research. The issues are discussed in more detail in sections 3–5 below.

Water plays a crucial role in PEM operation. The membrane must be well hydrated to have high protonic conductivity. However, too much liquid water can flood the gas channels or pores in the GDL or catalyst layer. *Water management* is the design of materials and operating conditions to produce sufficient liquid water to fully hydrate the membrane without flooding catalyst sites. This is a challenge to model since it involves a sensitive global coupling of electrochemistry with thermal and multiphase mass transport. Some aspects of water management are discussed in section 5 below.

The full reaction (2.1) releases approximately 1.5 joules per coulomb of electronic charge transferred and thus can be assigned a potential of 1.5 volts. If the anode and cathode are electrically isolated from each other, and no external current flows, then under ideal circumstances the two half-reactions will proceed until the charge in the double layers at the anode and cathode generates voltage jumps totaling approximately 1.2 volts, with the difference between the full reaction and the two half-voltages being the entropic losses. In this state the spatially complicated carbon/ionomer interface within the catalyst layers functions as a charged capacitor. However, various effects, particularly crossover of hydrogen gas through the polymer membrane, reduce actual "open circuit" potentials, E_o, to around 0.9 volts:

$$E_o = E_c - E_a, \tag{2.4}$$

where E_c and E_a are the cathode and anode contributions, represented in Figure 2.3. If the external electric circuit between the anode and cathode is completed, then the ORR causes the accumulated "capacitance" within the catalyst layer to be discharged, and loss of double-layer capacitance must be recharged dynamically. The relation between the anode and cathode reaction rates, $I_{a/c}$, and loss of voltage, or "overpotential" $\eta_{a/c}$, due to discharge of the capacitance is a fundamental characterization of the catalyst layer. At a macroscopic level this relation is given by the Butler–Volmer equations

$$I_c = \frac{i_{o,c}}{\mathcal{F}} \frac{c_O}{c_{O,\mathrm{ref}}} \left[\exp\left(\frac{\alpha_c \mathcal{F}}{\mathcal{R}T} \eta_c \right) - \exp\left(-\frac{\alpha_c \mathcal{F}}{\mathcal{R}T} \eta_c \right) \right], \tag{2.5}$$

$$I_a = \frac{i_{o,a}}{\mathcal{F}} \frac{c_H}{c_{H,\mathrm{ref}}} \left[\exp\left(\frac{\alpha_a \mathcal{F}}{\mathcal{R}T} \eta_a \right) - \exp\left(-\frac{\alpha_a \mathcal{F}}{\mathcal{R}T} \eta_a \right) \right]. \tag{2.6}$$

Here I_c and I_a are, respectively, the local electron consumption in the cathode and electron production in the anode, and c_O and c_H are the molar densities of oxygen and hydrogen at the respective catalyst sites. The factors $i_{o,c}$ and $i_{o,a}$ are the reference exchange currents for the anode and cathode catalyst layers, while $c_{O,\mathrm{ref}}$ and $c_{H,\mathrm{ref}}$ are reference densities. These four parameters give an effective macroscopic description of the catalyst layer microstructure. Faraday's constant, $\mathcal{F}$; the ideal gas constant, $\mathcal{R}$; and the local temperature, T, enter into the formula. The local density of hydronium, c_+, which also participates in the ORR (2.3), could be included in the Butler–Volmer relation; however, local electroneutrality effectively slaves the hydronium concentration to the local acid charge density which is essentially a material parameter. Consequently the local hydronium density is typically absorbed into the

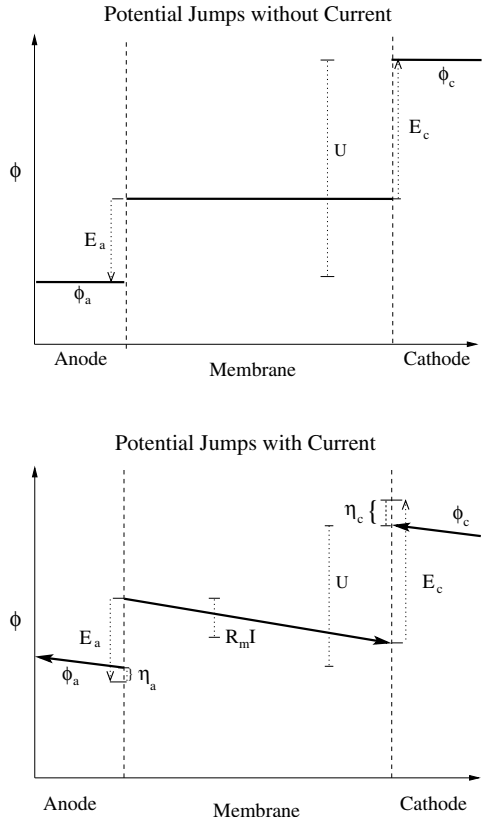

FIG. 2.3. *Schematic representation of the potential ϕ as a function of position over a single conductive pathway through the MEA. Top: No current is drawn, the potentials are flat, and the jumps at boundary layers are given by the half-electrode potentials, E_a and E_c, respectively, that sum to give the open circuit potential. Bottom: Current is drawn, the arrows show the direction of flow of electrons in the electrode and of protons in the membrane. The jumps at the catalyst layer are reduced by the overpotentials, η_a and η_c, that depend upon the transport of reactants through the GDL to the catalyst sites. The useful potential, U, given by* (2.7)*, is reduced, while the power production, UI, may increase from zero at open circuit conditions to a maximum before falling off at high current densities.*

exchange current density. A simple voltage balance relates the net voltage U produced by the cell to the kinetic reaction rate I:

$$U = E_o - \eta_c(I, c_O) - \eta_a(I, c_H) - R_m I, \tag{2.7}$$

where R_m represents an effective ohmic resistance of the MEA; see Figure 2.4 for a graphical representation of these quantities. The global coupling present in the problem is now relatively clear. The presence of liquid water greatly diminishes the membrane resistance, R_m, but excessive water will reduce the oxygen concentration c_O at the catalyst layer; moreover, the voltage difference $E_o - U$ generates waste heat at the rate $I(E_o - U)$, impacting the temperature profile and hence the phase change between liquid water and vapor. Furthermore, the consumption of oxygen and production of water vapor change the gas mixture substantially from inlet to outlet in the x direction, so that under typical conditions some regions of the cell operate in a dry regime, while others are in a two-phase regime.

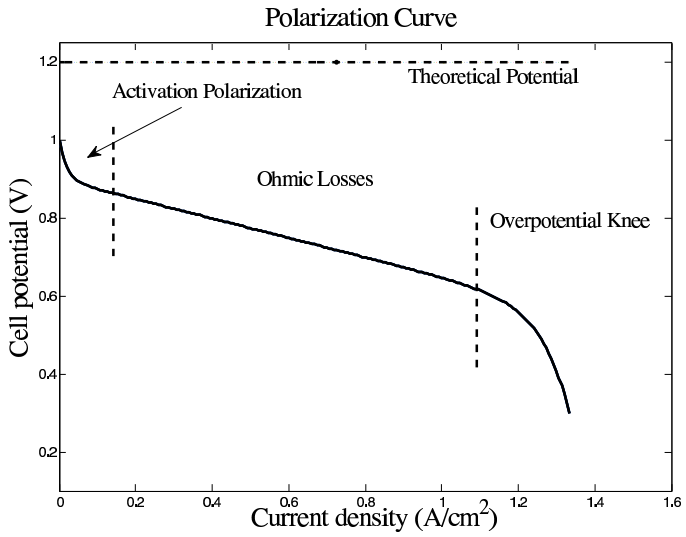

FIG. 2.4. *A typical polarization curve showing the current-voltage relation at fixed MEA water content, often called an instantaneous polarization curve. There is an initial drop in the cell potential due to activation polarization, followed by a long linear decay in voltage due to omhic losses, and then a sharp knee in the potential due to the inability to transport reactants to the catalyst sites, which can be due to liquid water accumulation.*

An individual cell often can provide no more than 0.6 volts at reasonable current densities, so to increase power production for automotive and large stationary applications, up to 100 or more unit cells are placed in series to form a fuel cell stack. In a stack configuration the anode plate of one cell is placed next to the cathode plate of the next so that their voltages will add. The combined plates are called *bipolar* plates. A sketch of a stack cross-section (x-z) is shown in Figure 6.3. Because the unit cells in a stack are arranged in series, the same total current passes through each of them. For this reason it is common to study individual unit cells as operating at a prescribed total current. In this situation the reactant gas inlet flows are typically measured as stoichiometric ratios (stoichs) of the flow that would provide exactly enough reactant to produce the prescribed current. Reactant gases and coolant are typically delivered to unit cells in a stack through header manifolds.

The discussion above focuses on typical current designs for PEM fuel cells for automotive or stationary applications, but there are other variants. Interdigitated cathode channel designs [119] have been shown to improve water management in certain situations. For portable power, the Ballard Nexa design does not have a separate coolant system; rather it is air cooled using a high oxidant flow rate. In addition it features dead-ended anode channels. Smaller unit cells for portable electronic devices can passively use ambient air and can also feature dead-ended anodes [58]. Some advantages in water management have been achieved by incorporating a porous material for the landing areas, so that liquid water can be introduced on the cathode inlet side and extracted from the anode outlet, effectively keeping the membrane fully hydrated along the length of the channel. This serves to break the intrinsically unstable feedback between membrane hydration and water production, permitting the cell to operate stably at very low anode stoichs; however, performance under repeated freeze-thaw cycles is unclear [57, 111]. These design variants use the same kind of

MEA construction, and so the discussion in sections 3–5 is generally applicable. However, the requirements for MEA design in these cases might be quite different from those of conventional systems.

There are several alternative approaches to fuel cells, quite different from PEM designs. The most similar are direct methanol fuel cells [72, 26] that are also low temperature and use similar MEA construction. However, they use a methanol and water mix for fuel and produce CO_2 gas as a by-product. Alkaline fuel cells [66] operate at an intermediate temperature. Both molton carbonate [115, 32] and solid oxide [43] fuel cells operate at high temperatures. In the previous citations, we have listed review articles and some selected papers of more mathematical interest.

Several themes in fuel cell modeling are reflected in this overview. The main mathematical theme is multiscale modeling and analysis. Changes in micro- and nanoscale structures in the MEA components can affect stack level performance. Appropriate stack level operating conditions can reduce or eliminate serious component material degradation effects. The main application issues are device cost and durability [12]. Thus, models are built to examine questions like How can we operate existing stacks most efficiently?; What are the bottlenecks to current performance and what material or system changes are necessary to bypass them?; What are the current lifetime limiting degradation effects in fuel cells and how can they be reduced by material improvements or operating conditions? An additional key issue for the commercialization of fuel cells is fuel (hydrogen) generation and storage, which is outside the scope of this article; see [91, 92, 23, 46].

3. Membrane models. The membrane which separates the cathode from the anode must serve several functions. First, it should efficiently conduct protons, while preventing electrons and reactant gases from crossing. Moreover, it must maintain structural integrity over a wide range of operating conditions, from freezing to 80°C for typical operating conditions, as well as under high compressive loads. Indeed there is considerable effort to develop a high-temperature cell that can operate at up to 120°C to improve carbon monoxide tolerance [101], simplify heat extraction, and increase catalytic performance of the ORR. Membranes which could retain conductivity and structural integrity above 200°C could lead to nonprecious metal catalysts. While polymer electrolyte membranes come in various forms, a common trait is a hydrophobic polymer backbone that has been functionalized by the addition of acidic sidechains. The industry standard is Nafion, a perfluorosulfonic acid, essentially repeating linear—CF_2—units with an occasional short sidechain terminating in an $-SO_3H$ acid group. In the presence of water (or other solvent) the hydrogen disassociates from the acid group, producing an electrolyte solution of H_3O^+ and tethered anions, SO_3^-. Other variants include PEEKs which replace the fluorocarbon backbone with a benzene ring. There are several variants of Nafion, with different equivalent weights (the weight in grams of membrane material which contains one mole of acid groups), sidechain lengths, spatial distributions of acid groups, and stiffness of the polymer backbone.

All of the polymer membranes absorb water, and their protonic conductivities increase with water content. As water is absorbed into the membrane, a phase separation occurs that forms a water-filled pore network which serves as the protonic conductors [77]. However, the absorption of water is relatively slow and is a very hysteretic process; see Figure 3.1 (bottom). Indeed Nafion has three identified states, expanded (E), normal (N), and shrunk (S) [40], depending upon its pretreatment, with transitions between these states requiring tens of hours to days of exposure. An

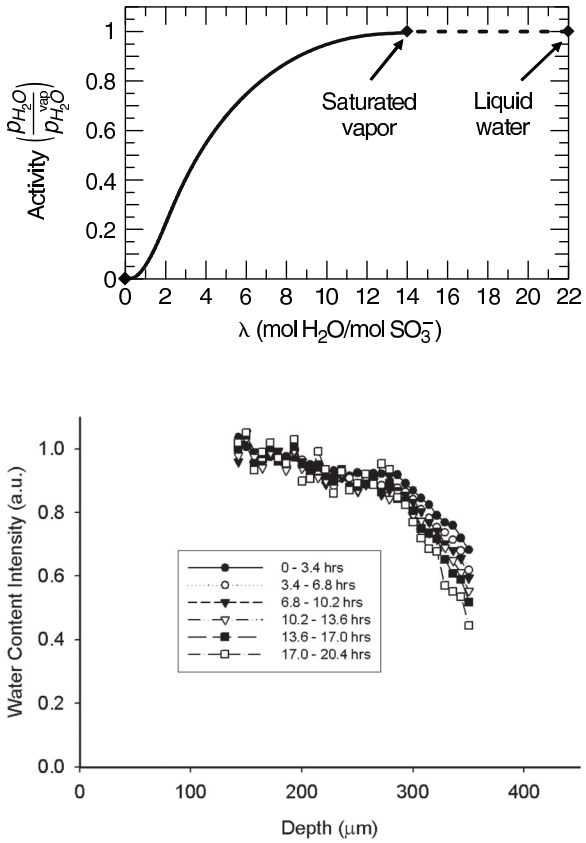

FIG. 3.1. *Top: The isotherms of Nafion in the normal form. Reprinted from* [*A. Z. Weber and J. Newman,* Modeling transport in polymer-electrolyte fuel cells*, Chem. Rev.,* 104 (2004)*, pp.* 4679–4726]. *Copyright* © 2004 *American Chemical Society. Reprinted with permission. All rights reserved. Bottom: An MRI image of the water content of a Nafion membrane exposed to liquid water on the left-hand side (*0–125 *micrometers) and water vapor, at* 30*% RH, on the right-hand side (*350–450*) micrometers. The water content is described by a piecewise linear function of position with much larger slope near the vapor equilibrated end. Moreover, the slope of the water content in the vapor equilibrated region changes significantly over a* 20*-hour transient, consistent with a slow rearrangement of the structure of the pore phase; see* [124] *for further details.*

identifying feature of any ionomer membrane is its water sorption isotherm that relates the adsorbed water molecules per acid group to external relative humidity (RH); see Figure 3.1 (top). Nafion has long been associated with the so-called Schroeder paradox in which considerably more water is adsorbed from a liquid water environment than from a saturated vapor environment (100% RH), in apparent contradiction to the chemical equilibrium between saturated vapor and liquid at the same temperature and pressure. The form of the adsorption isotherms has a leading order impact on the functioning of the membrane as its conductivity is strongly tied to its water content. Thus the initial observations of the Schroeder paradox have stimulated considerable experimental investigation, with a recent paper [75] suggesting that it is in fact yet another example of hysteresis, with liquid and vapor equilibrated membranes having a similar isotherm if their thermal pretreatment histories are similar.

A key mathematical issue is to determine the pore structure, protonic conductivity, and macroscopic behavior of PEMs from their fundamental characteristics:

equivalent weight and distribution of acid groups, backbone stiffness and hydrophobicity, and crosslinking of the polymer [78]. The overall goals are to understand the mechanics behind the hysteresis, to improve protonic conductivity, and to develop membranes that are stable and protonically conductive at temperatures well above 100°C. There has been significant computational investigation of polymer electrolytes at a variety of length scales; see [50] for a comprehensive review of this issue from the ab initio to the molecular dynamics level. The ab initio approach resolves electronic structure, computing the disassociation of acid groups and the interaction of small clusters of atoms. Molecular dynamics approaches model electronic interactions through averaged partial charges, but may resolve issues on a larger length scale, such as the formation of individual pores within the Nafion. Larger scale atomistic simulations, based upon density functional theory, lump groups of atoms together into effective particles (see [117]) and are capable of resolving networks of pores. However, none of these methods can approach the time scales on which the pore networks form and coarsen. Indeed this network coarsening is the mechanism that yields the hysteresis which is fundamental to Nafion's behavior. At the macroscopic level, when resolving length scales greater than a micrometer, there are a wide range of modeling efforts that attempt to predict water distributions in a Nafion membrane from anode to cathode under various operating conditions, including the elastic response to external pressures; see [114] for a nice overview. Efforts have been made to include both pressure and diffusive driven water transport [109], to explain the Schroeder paradox from chemical isotherms [20], and to study membranes under elastic compression [110, 71]. These efforts evoke a pre-existing pore structure to motivate classes of macroscopic models and to attempt to fit known behavior through the adjustment of various control parameters.

3.1. Phase separation in functionalized membranes. In this section we outline a class of continuum level models for the pore formation within polymer electrolytes based upon novel extensions of the classical Allen–Cahn and Cahn–Hilliard energies [17]. Rather than viewing the pores as static features of the membrane, we describe them as a dynamic phase separation process. The polymer backbones are hydrophobic and do not mix freely with water. To generate a nanoscale pore structure, the immiscibility of the polymer and water is reversed by the *functionalization process*, that is, the addition of the acid-terminated sidechains, effectively embedding latent energy within the polymer, energy that is released upon the formation of the polymer-solvent interface. The proposed model exploits a fundamental structure implicit in the functionalization of the polymer backbones, balancing energy liberated by hydration and proton dissociation of the hydrophilic sidechains against elastic bending moments of the hydrophobic backbone polymer. The energy liberated by the hydration of the acid groups is proportional to the surface area of the water-polymer interface. In a phase field model with a smooth phase function taking the values $\psi = \pm 1$ in water and polymer domains, respectively, and with small parameter ϵ representing interfacial width, the surface area can be modeled by the Allen–Cahn energy

$$\mathcal{A}(\psi) = \int_\Omega \epsilon \frac{1}{2} |\nabla \psi|^2 + \epsilon^{-1} W(\psi) dx, \tag{3.1}$$

where $W(s) = \frac{1}{4}(1 - s^2)^2$ is a double-well potential. However, the functionalized polymer chains are effectively bonded, via the disassociated acid groups, to the water-filled pores, forming a sheath around them and imbuing the pore with an elasticity;

see Figure 3.3(b) for a depiction. The water-polymer interface attempts to minimize free energy by *maximizing* its interfacial area; however, this intrinsically unstable dynamic is regularized by the elastic deformation of the backbone sheath, whose energy is proportional to the square of the curvature of the interface, which is also the square of the variational derivative of $\mathcal{A}$,

$$\mathcal{H} = \frac{1}{2}\int_\Omega \left(\frac{\delta \mathcal{A}}{\delta \psi}\right)^2 dx = \frac{1}{2}\int_\Omega \left(\epsilon \Delta \psi - \epsilon^{-1} W'(\psi)\right)^2 dx. \tag{3.2}$$

The Γ-convergence of $\mathcal{H}$ to the Willmore functional as $\epsilon \to 0$ has been shown; see [63]. With $\eta > 0$ describing the relative energy densities of the acid disassociation and the backbone stiffness, the interfacial energy is given by the balance

$$\mathcal{I} = \mathcal{H}(\psi) - \eta \mathcal{A}(\psi). \tag{3.3}$$

This novel energy is naturally fourth order, but is imbued with a rich structure from its special form. Indeed, quite generally we may define the *quadratic functionalization* $\mathcal{F}$ of an energy $\mathcal{E}$ by

$$\mathcal{F}(\psi) \equiv \frac{1}{2}\int_\Omega \left(\frac{\delta \mathcal{E}}{\delta \psi}\right)^2 dx - \eta \mathcal{E}(\psi). \tag{3.4}$$

The functionalized energy has a first variational derivative with twice the differential order of the original energy, but this higher-order variation factors as

$$\frac{\delta \mathcal{F}}{\delta \psi} = \frac{\delta^2 \mathcal{E}}{\delta \psi^2}\frac{\delta \mathcal{E}}{\delta \psi} - \eta \frac{\delta \mathcal{E}}{\delta \psi} = \left(\frac{\delta^2 \mathcal{E}}{\delta \psi^2} - \eta\right)\frac{\delta \mathcal{E}}{\delta \psi}. \tag{3.5}$$

It has been shown [88] that, for a general class of second-order energies, the associated quadratic functionalization possesses global minimizers that are solutions of the associated Euler–Lagrange equations. From the factored form of the Euler–Lagrange equations, it is clear that $\mathcal{F}$ also inherits the critical points of $\mathcal{E}$; however, the second variation of $\mathcal{F}$ at a critical point $\psi_\mathcal{E}$ of $\mathcal{E}$ takes the form

$$\frac{\delta^2 \mathcal{F}}{\delta \psi^2}(\psi_\mathcal{E}) = \left(\frac{\delta^2 \mathcal{E}}{\delta \psi^2} - \eta\right)\frac{\delta^2 \mathcal{E}}{\delta \psi^2}. \tag{3.6}$$

A critical point $\psi_\mathcal{E}$ of $\mathcal{E}$ is a local minimizer of $\mathcal{F}$ if and only if its second variation is positive definite, and it has been shown that this requires that the second variation of $\mathcal{E}$ at $\psi_\mathcal{E}$ not have spectrum in the interval $(0, \underline{\eta})$, where $\underline{\eta}$ is a lower bound on η. While the critical points of $\mathcal{E}$ are local minimizers of $\mathcal{F}$ for small η, for a large class of energies $\mathcal{E}$ one can choose η sufficiently large, so that all critical points of $\mathcal{E}$ are saddles of $\mathcal{F}$, and the global minimizer of $\mathcal{F}$ is necessarily a new structure, generically a network, that is born of the functionalization. In this manner, by adjusting the balance parameter η, the minimizers of $\mathcal{E}$ can be stabilized or destabilized, and network structures corresponding to the large η minimizers of $\mathcal{F}$ can be generated in a controlled manner. The study of these minimizers, and more generally minimizers subject to constraints, such as prescribed volume fraction, is an open and interesting problem.

In the model at hand, the interfacial energy $\mathcal{I}$ is the functionalization of surface area represented through the Allen–Cahn energy. Natively the hydrophobic backbone seeks to minimize the surface area of its interface with water. However, when the

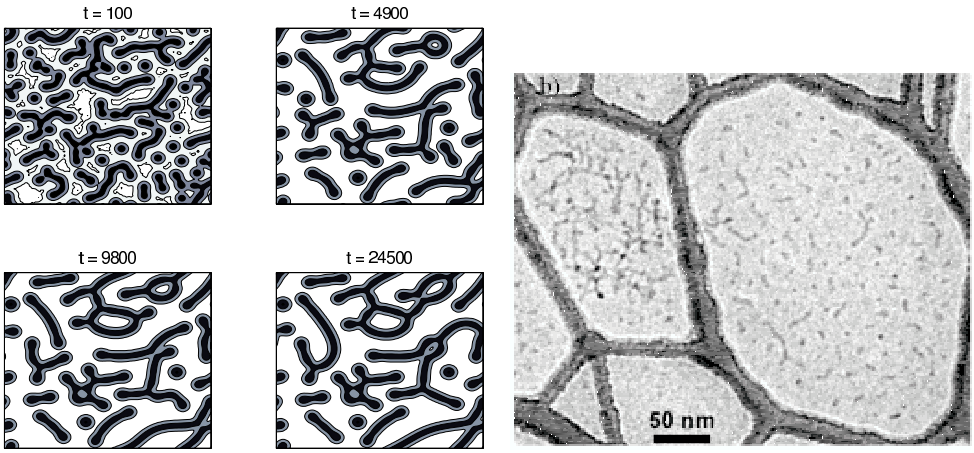

FIG. 3.2. *Left: A two-dimensional (2D) simulation of a gradient flow of form* (3.7) *with* $\rho = 1$ *and with periodic boundary conditions for an* 80% *polymer (white) and* 20% *solvent (dark) mixture starting from "boiled" initial data, with zero mean white noise added at each time step. Parameters are* $\epsilon = 2\times10^{-2}$, $\eta = 2\epsilon$. *Right: Cryo-transmission electron microscopy (TEM) image of Nafion* 1100 *solution. Reprinted from* [*L. Rubatat, G. Gebel, and O. Diat,* Fibrillar structure of Nafion: Matching Fourier and real space studies of corresponding films and solutions*, Macromolecules,* 37 (2004)*, pp.* 7772–7783]. *Copyright* © 2004 *American Chemical Society. Reprinted with permission. All rights reserved. The authors describe the solvent phase as "a network of wormlike structures." The lateral width of the image is roughly* 100 *nanometers. Dark spots are water, and brighter regions depict crystallized Nafion. The thick black lines are carbon inclusions that support the membrane.*

polymer has been functionalized by the addition of acidic sidechains, the nature of the polymer-water interaction is reversed and it becomes exothermic. The generation of interface is regularized by the square of the variational derivative of surface area, producing an interfacial energy with a rich class of critical points, including global minimizers, local minimizers, and saddle points. Heating the polymer membrane softens the backbone material while leaving the density of the embedded acid groups fixed; heating thus increases the value of η. The hysteresis under heating and cooling that is so prevalent in the polymer electrolytes is a function of the destabilization and restabilization of the various local minimizers, generating the pore network associated with the large η global minima. This process is not restricted to synthetic materials: proteins are an important class of functionalized polymer, natively hydrophobic but with many embedded charges that encode their particular chemical purpose. Chief among these purposes is the formation of ion channels, which are more sophisticated forms of phase separated polymer electrolytes, with higher acid density and more sensitive ion selectivity.

The simplest, physically reasonable flows associated with the interfacial energy are the mass-conserving gradient flows

$$\psi_t = -\mathcal{G}_\rho \frac{\delta \mathcal{I}}{\delta \psi} = -\epsilon^{-2}\mathcal{G}_\rho \left(\epsilon^2\Delta - W''(\psi) - \epsilon\eta\right)\left(\epsilon^2\Delta\psi - W'(\psi)\right), \tag{3.7}$$

where $\mathcal{G}_\rho = -(1+\rho)\Delta/(I-\rho\Delta)$ is a gradient that ranges from the Laplacian, $\mathcal{G}_0 = -\Delta$, to the negative of the zero-mass projection, $\mathcal{G}_\infty f = -(f - \langle f\rangle_\Omega)$, as ρ runs from 0 to ∞. A typical simulation corresponding to period boundary conditions in a square domain Ω is presented in Figure 3.2. The flow starts from an initial condition corresponding to a glassy state (boiled) and shows the coarsening of the pore structure

for the cooled sample with a decreased value for η. The gradient flows (3.7) will also spontaneously form fine-structured interfaces from large-scale mixtures of polymer and water, absorbing the water into the polymer and forming a pore network.

The $\mathcal{G}_0$ gradient flow for Allen–Cahn energy, $\mathcal{A}$, is just the Cahn–Hilliard equation

$$\psi_t = \Delta(\epsilon^2 \Delta\psi - W'(\psi)). \tag{3.8}$$

When subject to zero-flux boundary conditions, the Cahn–Hilliard equation supports a large family of quasi-steady front solutions that take the form $\psi = \pm 1$ on $\Omega_\pm$, where Ω is the disjoint union of Ω_+ and Ω_-, with a smooth transition front supported in an ϵ neighborhood of the simple curve $\Gamma = \partial\Omega_+ \cap \partial\Omega_-$. Both formally and rigorously [83, 1], it has been shown in the $\epsilon \to 0$ limit that the normal velocity of the interfacial curve Γ is given by a Mullins–Sekerka flow; that is, if we define $v_\pm$ in $\Omega_\pm$ by

$$\begin{aligned} \Delta v_\pm &= 0, && \Omega_\pm, \\ \nabla_n v_\pm &= 0, && \partial\Omega \cap \partial\Omega_\pm, \\ v_\pm &= -\tfrac{S}{2}\kappa, && \Gamma, \end{aligned} \tag{3.9}$$

where S is the surface tension and κ is the mean curvature of the interface, then the normal velocity, V, of the interface Γ is proportional to the jump in the normal derivative,

$$V = \frac{1}{2}\left[\!\left[\nabla_n v_\pm\right]\!\right], \tag{3.10}$$

along Γ. Thus the mean curvature drives the flow, smoothing the interface. For the $\mathcal{G}_0$ flow of the functionalized interface energy, the front solutions are no longer stable, at least for $\eta = O(\epsilon)$; however, the front evolution is still slow. There is still a sharp interface limit corresponding to a Mullins–Sekerka-type flow, but the driving force is *against* the interface curvature, regularized by the surface Laplacian (Laplace–Beltrami operator) Δ_s, but destabilized by nonlinear terms,

$$\begin{aligned} \Delta v_\pm &= 0, && \Omega_\pm, \\ \nabla_n v_\pm &= 0, && \partial\Omega \cap \partial\Omega_\pm, \\ v_\pm &= \tfrac{S}{2}\left((\Delta_s + \eta)\kappa + \tfrac{1}{2}\kappa^3\right), && \Gamma. \end{aligned} \tag{3.11}$$

These equations govern the initial stages of instability of a front-type solution until the fingering instability generates the pore structure. The subsequent evolution of the pore structure is currently an open problem.

3.2. Conductive polymer electrolyte equations. A broader goal is to incorporate elastic and electrostatic energy into models for the macroscopic behavior of the membrane material and to build in Angstrom scale effects, such as the solvation of ions by water, upon the proton conduction. The elastic deformations of PEMs are strongly coupled to the ion conduction and water adsorption [51]. Indeed there are efforts to use polymer electrolytes as actuators and sensors by either driving ionic currents through an unconstrained membrane to cause it to bend, or by measuring the ion flux that results from an elastic impulse; see [73, 95] for modeling efforts in these directions. Within the context of PEM fuel cells the membrane is constrained between the anode and cathode flow-field channels and is limited in its ability to swell,

which may significantly impact water adsorption (see [110, 71]) and even lead to oscillations and bifurcations [4]. Moreover, lateral variations in water content can lead to strain that, when coupled with the thermal cycling typical in automotive applications, may result in tearing or perforation of the membrane, which is a significant source of degradation [53, 39, 12]. Water that freezes in the backing layers of the MEA may generate elastic stresses which can contribute to degradation in shut-down and start-up at subzero temperatures. Thus, there are many connections between membrane mechanical degradation and water management.

The Department of Energy has led a significant push to develop PEMs that function at higher temperatures (120–150°C) to increase the tolerance to carbon monoxide, a common impurity in hydrogen gas obtained from reformed hydrocarbons, and to facilitate heat extraction. Also, maintaining an automotive PEM fuel cell at 80°C against an ambient temperature of 30–40°C requires a significantly larger radiator than does the internal combustion engine which operates at higher temperatures, and the coolant issue is currently a limitation in PEM operating efficiency. More significantly, higher operating temperatures will open the door to nonprecious metal catalysts for the ORR, which would significantly reduce production costs. However, at higher operating temperatures current PEMs undergo a glass transition and lose their structural integrity, leading to viscoelastic flow and potential membrane rupture. Also, higher temperature increases rates of membrane degradation and carbon corrosion. The viscoelastic flow of the membrane has been investigated experimentally [53]; however, the most systematic attempts to incorporate membrane stress into the membrane's overall response have occurred in the actuator literature [73, 95].

To address these issues we extend a general class of phase-field models based upon a momentum balance that has been proposed by Liu for fluid-elastic mixtures; see [60, 59, 28]. These possess a favorable energy structure and handle the Eulerian–Lagrangian dichotomy of the fluid flow versus the elastic response of the membrane material by pulling the Lagrangian evolution back into an Eulerian framework. To handle the elastic energy, one observes that for a deformation $x = x(X,t)$ of the elastic structure, from an "unstressed" reference configuration ψ_{ref} in terms of X, the Lagrangian coordinate, the velocity $v = x_t$, and the deformation gradient $F = \frac{\partial x}{\partial X}$ must satisfy a compatibility equation, essentially the chain rule, with the velocity,

$$F_t + v.\nabla F = (\nabla v)F. \tag{3.12}$$

The elastic energy, $\mathcal{W}(F)$, may be taken as a generic nonlinear functional of the deformation F.

Our extension should couple the evolution of the charged polymer-water interface to Poisson's equation in such a way as to preserve energy dissipation. Moreover, proton conduction in water is somewhat nonstandard as the excess proton is effectively an extra hydrogen bond in a hydrogen bond network. The density of hydrogen bonds within the water phase correlates strongly with the relative permittivity of the water, which is typically low in the vicinity of the interface, where the waters hydrate the pendant acid groups, and much higher within the middle of the pore, where the water is more bulk-like; see Figure 3.3. This discussion suggests that both hydrogen bond density, $h = h(\psi)$, and the dielectric constant, $\varepsilon = \varepsilon(\psi)$, be taken as prescribed functions of the phase-field variable ψ, low where $\psi = -1$ and high where $\psi = 1$. The Gibbs–Boltzmann entropy for this mixture is modified to incorporate the

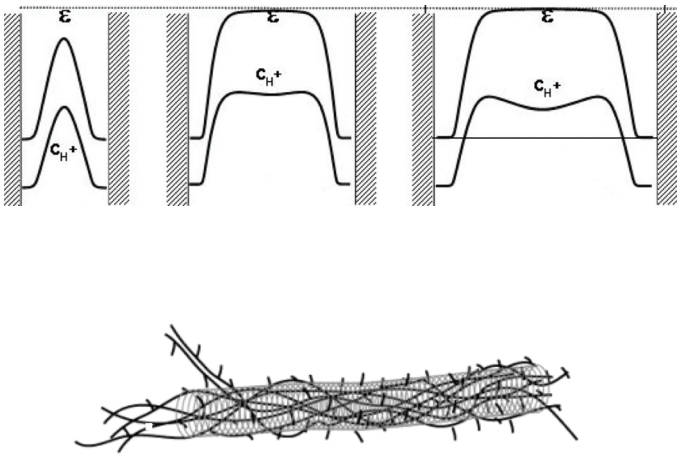

FIG. 3.3. *Top: Profiles of the dielectric constant and protonic charge carrier concentration in a hydrated hydrophilic channel (pore) at three different water contents. Reprinted from* [*K.-D. Kreuer, S. J. Paddison, E. Spohr, and M. Schuster,* Transport in proton conductors for fuel-cell applications: Simulations, elementary reactions, and phenomenology, *Chem. Rev.,* 104 (2004), *pp.* 4637–4678]. *Copyright* © 2004 *American Chemical Society. Reprinted with permission. All rights reserved. Segregation of cationic and anionic charges leads to exceptional proton mobility. The entropic force resulting from low hydrogen bond availability excludes the protonic defects from the wall; see also* [76, 80, 81, 82]. *Bottom: An interpretation, from Rubatat and Diat, of the structure of Nafion channels based upon small angle scattering (SAX) and TEM scattering data. Reprinted from* [*L. Rubatat, G. Gebel, and O. Diat,* Fibrillar structure of Nafion: Matching Fourier and real space studies of corresponding films and solutions, *Macromolecules,* 37 (2004), *pp.* 7772–7783]. *Copyright* © 2004 *American Chemical Society. Reprinted with permission. All rights reserved. The hydrophobic backbones form a sheath around the pore, effectively glued on by the hydrophilic sidechains. Earlier work of Hsu and Gierke* [41] *postulated that a balance of elastic deformation and hydrophilic surface interactions leads water to form spherical hydrophilic clusters of* 4*-nanometer radius surrounded by sulfonate groups, with the clusters connected through cylindrical channels of* 1*-nanometer diameter.*

nonuniformity of the hydrogen bond lattice upon which the protons walk,

$$\mathcal{S}(p,\psi) = \int_\Omega p \ln \frac{p}{h}\,\mathrm{dx}. \tag{3.13}$$

The tethered $-SO_3H$ acid groups disassociate into negative ions and protons in the presence of water, and the negative ions ($-SO_3^-$) cluster along the polymer-water interface. Assuming full disassociation of the acid groups, it is reasonable to prescribe the local density of negative ions as a function $\hat{n}(\psi)$ of phase-field function, $n = n_0\hat{n}(\psi)/\int_\Omega \hat{n}(\psi)\mathrm{dx}$, normalized so as to conserve the average charge density n_0. Setting various physical constants to 1 for the remainder of this section, we introduce the action $\mathcal{G}$, which incorporates the entropy, interfacial energy $\mathcal{I}$ from (3.3), kinetic energy, elastic energy $\mathcal{W}$, and electrostatic Lagrangian $\mathcal{N}$, as functions of the local proton density p, the phase function ψ, the electric potential ϕ, the local mixture velocity v, and the deformation F:

$$\mathcal{G}(p,\psi,\phi,v,F) = \mathcal{I}(\psi) + \mathcal{S}(p,\psi) + \mathcal{W}(F) - \mathcal{N}(p,\psi,\phi) + \frac{1}{2}\int_\Omega |v|^2\mathrm{dx}. \tag{3.14}$$

The electrostatic Lagrangian is given the form

$$\mathcal{N}(p,\psi,\phi) = \int_\Omega \frac{1}{2}\varepsilon(\psi)|\nabla\phi|^2 - (p - n(\psi))\phi \,\mathrm{dx}, \tag{3.15}$$

so that the critical points of $\mathcal{N}$ with respect to the electric potential ϕ solve Poisson's equation

$$\nabla\cdot(\varepsilon(\psi)\nabla\phi) = -(p - n(\psi)). \tag{3.16}$$

Solutions of Poisson's equation are also critical points of the action

$$\frac{\delta\mathcal{G}}{\delta\phi} = \nabla\cdot(\varepsilon(\psi)\nabla\phi) + (p - n) = 0. \tag{3.17}$$

The free energy, $\mathcal{E}$, is obtained by requiring that ϕ maximize $\mathcal{G}$, i.e., solve Poisson's equation, in effect taking the Legendre transform of the action with respect to the electric potential. Using (3.16) to eliminate $p-n$ from (3.15) and integrating by parts, we obtain

$$\mathcal{E}(p,\psi,v,F) = \mathcal{I}(\psi) + \mathcal{S}(p,\psi) + \mathcal{W}(F) + \frac{1}{2}\int_\Omega \left[\varepsilon(\psi)|\nabla\phi|^2 + |v|^2\right] \mathrm{dx}. \tag{3.18}$$

The action may now be employed to generate a flow which dissipates the energy. The evolution for the phase field couples the interfacial and electrostatic energies with the entropy:

$$\begin{aligned}\psi_t + v.\nabla\psi = \Delta\frac{\delta\mathcal{G}}{\delta\psi} = \Delta\Bigg(\left(\frac{\delta^2\mathcal{A}}{\delta\psi^2} - \eta\right)\frac{\delta\mathcal{A}}{\delta\psi} - \frac{ph'}{h} \\ - \left[\frac{1}{2}\varepsilon'|\nabla\phi|^2 + n(\ln\hat{n})'\left(\phi - \int_\Omega \frac{n\phi}{n_0}\mathrm{dx}\right)\right]\Bigg),\end{aligned} \tag{3.19}$$

where $'$ denotes the derivative of a function of one variable with respect to that variable. The proton density evolves according to a modified Poisson–Nernst–Planck (PNP) equation which incorporates the entropic effects,

$$p_t + v.\nabla p = \nabla\cdot\left(p\nabla\frac{\delta\mathcal{G}}{\delta p}\right) = \nabla.\left(h\nabla\frac{p}{h} + p\nabla\phi\right). \tag{3.20}$$

The balance of momentum takes the form

$$v_t + v.\nabla v + \nabla\pi = \nabla\cdot(\mu(\psi)\nabla v) + \frac{\delta\mathcal{G}}{\delta\psi}\nabla\psi + \frac{\delta\mathcal{G}}{\delta p}\nabla p + \nabla\cdot(\mathcal{D}\mathcal{W}F^t), \tag{3.21}$$

where π is the pressure conjugate to the incompressibility, $\nabla.v = 0$, and $\det(F) = 1$. The viscosity, μ, is also taken to be a prescribed function of the phase-field variable ψ. In conjunction with Poisson's equation (3.16) and the compatibility condition (3.12), (3.19)–(3.21) are a closed system whose evolution dissipates the energy

$$\frac{d\mathcal{E}}{dt} = -\int_\Omega \left[\left|\nabla\frac{\delta\mathcal{G}}{\delta\psi}\right|^2 + p\left|\nabla\frac{\delta\mathcal{G}}{\delta p}\right|^2 + \mu(\psi)|\nabla v|^2\right] \mathrm{dx} \le 0. \tag{3.22}$$

They also conserve the mass of each phase and the charge densities.

We remark that in the modified PNP equation (3.20) it is the protonic entropy p/h that effectively diffuses, resulting in an apparent "entropic force" that serves to localize the protonic defects in the middle of the channel, away from the polymer-water interface:

$$p_t + v.\nabla p = \nabla.\left(\nabla p + p\nabla\phi - \overbrace{p\nabla \ln h}^{Entropic\ Force}\right). \tag{3.23}$$

The equilibrium solutions of this equation should be compared to the proton distributions, c_{H^+}, computed via a density functional approach in [50] and depicted in Figure 3.3.

3.3. Quasi-static ion conduction. The electrostatic and charge transport equations are much faster to equilibrate than the interfacial energy. If we take the phase separation ψ as fixed on the time scale of the charge transport, then under zero flux conditions the proton density p and electric potential ϕ are determined by the elliptic system

$$\nabla \cdot (\varepsilon(\psi)\nabla\phi) = n - p, \tag{3.24}$$

$$\nabla \cdot I = 0, \tag{3.25}$$

where the protonic current I takes the form

$$I = \nabla p + p\nabla\phi - p\nabla \ln h = p\nabla\left(\phi + \ln\frac{p}{h}\right). \tag{3.26}$$

In the absence of a driving force, such as an externally imposed electric field, not only is the divergence of the current zero, but the current itself is zero. The charge distribution becomes a function of the electric field,

$$p = p_0 h e^{-\phi}, \tag{3.27}$$

and Poisson's equation reduces to a modified Poisson–Boltzmann equation

$$\nabla \cdot (\varepsilon(\psi)\nabla\phi) = n - p_0 h(\psi) e^{-\phi}. \tag{3.28}$$

The solvability of the modified Poisson–Boltzmann equation is equivalent to global electroneutrality,

$$\langle n\rangle_\Omega = \langle p\rangle_\Omega, \tag{3.29}$$

that determines the constant p_0. The resulting quasi-steady conductive polymer electrolyte (CPE) equations consist of (3.19), (3.21), the incompressibility conditions, and the modified Poisson–Boltzmann equation (3.28).

At equilibrium, with zero velocity field, v, and stationary phase-field variable, $\psi = \psi(x)$, we may homogenize over a micrometer scale domain Ω to obtain an effective conductivity tensor $\overline{\sigma}$ that relates the averaged current density to the averaged potential gradient,

$$\langle I\rangle_\Omega = \overline{\sigma}\langle\nabla\phi\rangle_\Omega. \tag{3.30}$$

With an external driving force substantially weaker than the local electrostatic forces, the protonic charge density is determined from the phase field variable $p = p(\psi)$. The

potential can be written as a static and a dynamic part, $\phi = \phi_0 + \phi_d$, with the static coming from the modified Poisson–Boltzmann equations and the current given by the linear remnant of the proton transport equations

$$I = p\nabla\phi_d. \tag{3.31}$$

Equation (3.31) amounts to a high-contrast conductivity problem since the ion density p varies sharply with the hydrogen bond network density h. A network approach for high-contrast conductivity problems has been developed [10] that is well suited to the ion transport modeling of polymer electrolytes. The effective conductivity is known to have a variational formulation

$$\sum_{i,j=1}^{3} \overline{\sigma}_{ij}\xi_i\xi_j = \min_{\langle\nabla\phi_d\rangle=\xi} \langle p(\psi)\nabla\phi_d \cdot \nabla\phi_d\rangle_\Omega\,, \tag{3.32}$$

where ξ is an arbitrary vector in $\mathbf{R}^3$. In the high-contrast limit the analysis of this homogenization problem amounts to a study of the saddle points of the effective conductivity, parameterized here by the local proton density p, which is lowest at junction points where conductive channels meet and pinch down.

4. Catalyst layer models. The catalyst layer is the functional core of the PEM fuel cell. The partial reactions which occur on the surface of the catalyst generate the double layers which yield the cell's voltage. During the operation of the cell, the recharging of the double layers requires transport of molecular oxygen, protons, and electrons to the catalyst sites, each by a different transport route. The production of a catalyst ink with the requisite structure is the black art of fuel cell production, and many groups are experimenting with different formulations.

The state of the art catalyst layer for PEM fuel cells is a triply percolating mixture of polymer electrolyte, carbon support, and gas pores. The carbon support is comprised of 30–40 nanometer carbon black particles with 5–10 nanometer Pt catalyst inclusions decorating the surface. The carbon particulates naturally congregate into 150–250 nanometer agglomerates due to residual charges and surface interactions. The agglomerated carbon is mixed with an aqueous polymer alcohol solution forming the catalyst ink which is typically applied to the PEM fuel cell in a 10–20 micrometer film. After the mixing process, the alcohol evaporates, leaving residual pores. The Pt particles serve to catalyze the oxygen reduction half-cell reaction, which is both the most sluggish electrochemical reaction in the cell and the power source for the cell. The polymer electrolyte serves to conduct protons to the Pt sites, while the carbon agglomerate phase is the electron conductor, and the gas pores act as a conduit for molecular oxygen. The protons arrive from one side of the thin catalyst film, while the oxygen and electrons arrive from the other. At high reaction rates difficulty in transporting any one of the three reactants leads to loss of power and efficiency. Degradation of the catalyst ink, either by oxidation of the carbon support material or by migration and dissolution of Pt particles, reduces the effective Pt surface area available for reaction. Degradation effects pose significant limitations to PEM fuel cell longevity and are a significant obstacle to PEM fuel cell penetration into the automotive market.

The first micron-scale model of a PEM catalyst layer based upon effective transport parameters was proposed by Cutlip [22] in 1975, and in the ensuing 30 years this effort has branched into a wide range of agglomerate and macrohomogeneous models which include multiphase behavior at various levels (see [8, 6, 15, 29, 42, 56, 64,

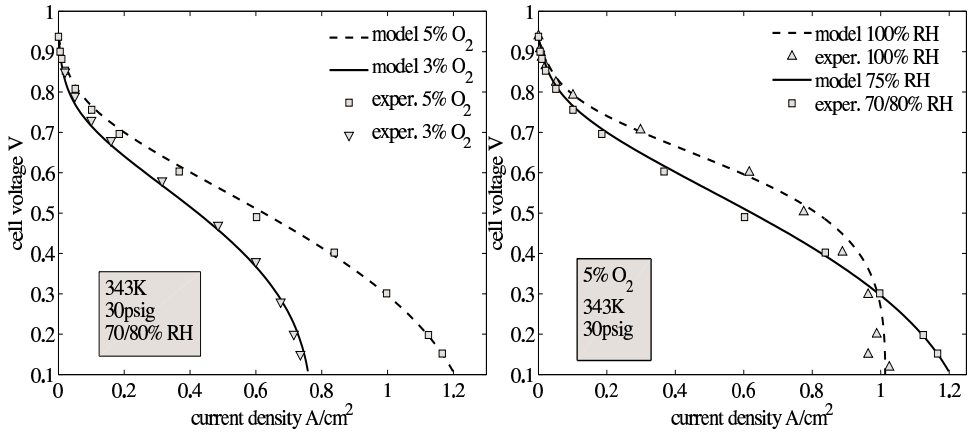

FIG. 4.1. *Polarization curves showing agreement between experimental and model predictions for polarization curves at different levels of oxygen concentration and humidity. Reprinted from* [*A. Shah, G. S. Kim, W. Gervais, A. Young, K. Promislow, J. Li, and S. Ye,* The effects of water and microstructure on the performance of polymer electrolyte fuel cells*, J. Power Sources,* 160 (2006)*, pp.* 1251–1268]. *Copyright* © 2006 *Elsevier B.V. Reprinted with permission. All rights reserved. The high humidity case gives better performance at low current density, but leads to flooding and an earlier knee than the lower RH system; see* [94] *for full details.*

65, 97, 98, 99, 94, 104, 107, 116]), including numerical simulation of AC impedance spectra [30] and [38]. There have also been studies which assume a simplified catalyst layer structure and attempt to extract performance; see [84]. These models have had success at resolving catalyst layer performance at the micron scale (see Figure 4.1), suggesting differential Pt loadings across the thickness of the catalyst layers to improve performance. However, the models share a major limitation with Cutlip's original model: They do not resolve the phase separation which occurs at the 5–150 nanometer length scale. This nanoscale structure defines the catalyst layer and determines its performance. True improvement in catalyst layer performance and longevity requires understanding and control of structure on this length scale [68].

4.1. Catalyst layer preparation models. Catalyst layers are formed by mixing a nanodispersed carbon support powder, previously decorated with 5–10 nanometer platinum inclusions, with an aqueous solution of perfluorosulfonic acid polymer and isopropyl alcohol which serves as a binder and proton conductor. The structural distribution of carbon support/gas phase/ionomer phase of the resulting mixture determines the effective Pt surface area of the catalyst ink. Agglomeration of carbon support is essential to achieving a high effective electronic conductivity; however, interpenetration of ionomer within the agglomerates enhances protonic conductivity to the active Pt sites, while a pore network is needed to conduct molecular oxygen to a proximity of Pt reaction sites. Moreover, the centers of large agglomerations of carbon support material are inefficient reaction sites and will not contribute appreciably to effective Pt surface area. The models must predict the impact of carbon support surface wettability and intercarbon attractivity as well as ionomer viscosity and volume fraction on the configurational form of the end-state catalyst/ionomer mixture. The second stage of the preparation is the drying process, in which the evaporating alcohol leads to cracking and residual pore formation.

Such models could be built from the framework of the CPE models, (3.19)–(3.21), starting with a vector-valued phase-field function ψ which takes values in $\mathbf{R^3}$, with

four distinguished states $\psi_s, \psi_g, \psi_i, \psi_l$ located on the corners of a tetrahedron and corresponding to solid, gas, ionomer, and liquid regimes. The associated interfacial energy takes the form

$$\mathcal{A} = \int_\Omega \frac{\epsilon}{2}|\nabla\psi|^2 + \frac{1}{\epsilon}F(\psi)dx, \tag{4.1}$$

where F has local minima at each of the four distinguished states and a local maxima at the origin. This formulation admits interfaces between any two of the four phases, with the interfacial energy dependent upon the height of the saddle point connection. Agglomeration of carbon support particles is driven by residual charges and weak surface bonding which can be modeled by a van der Waals type potential:

$$\mathcal{N}(x) = \begin{cases} \sum_{k\neq k_0}^{N_c} \left(\dfrac{\alpha}{|x_k - x|^M} - \dfrac{\beta}{|x_k - x|^N} \right), & x \in C_{k_0}, \\ 0, & x \notin \cup_{k=1}^{N_c} C_k, \end{cases} \tag{4.2}$$

where $\alpha, \beta > 0$, $M > N > 0$, and x_k for $k = 1, \ldots, N_c$ denotes the center of mass of the kth catalyst support particle, $C_k \subset \mathbf{R^3}$. Including the gradient of $\mathcal{N}$ on the right-hand side of (3.21) incorporates interparticle attractivity into the model in a natural way. The existence and stability of traveling waves which connect two or more of the phases as well as the Γ convergence of $\mathcal{A}$ as $\epsilon \to 0$ are areas of active research (see [2]), as is the proper functionalization of $\mathcal{A}$.

4.2. Catalyst layer performance models. The performance of a catalyst layer is typically characterized by its effective Pt surface area (EPSA) or, more directly, by voltage losses under various operating conditions. Optimization of performance over the full range of possible catalyst layer structures is an ambitious task. Even the direct problem of accurately predicting performance from material composition is complicated by the range of length scales present and the variability in structure due to accumulation of liquid water, the associated swelling of the ionomer phase, and the resultant variability in pore distributions and proton conductivity. The performance models must simulate mass and heat transfer in the catalyst layer, including the impact of liquid water generation and phase change. In particular the models must resolve the distribution of water both as liquid within the agglomerates and in its bound state within the ionomer phase, determining its impact on proton, oxygen, and electron transport as well as contributions to structural rearrangement within the catalyst/ionomer mixture. Resolving transport over the 5–500 nanometer range will permit determination of effective transport parameters and their dependence on nanostructure and hydration level. The models should be validated against AC impedance spectra and voltage sweeping, and by comparison of predicted interparticle and interagglomerate spacing as a function of hydration level with direct measurements by in situ small-angle x-ray scattering experiments.

The presence of the electrochemical reactions and the associated change of phase represent the major distinction between the performance and preparation models. The phases must be tracked, as well as the species within each phase. In the gas phase the mole fractions of oxygen, water vapor, and nitrogen have essential impact on the reaction rates. In the liquid phase, the density of both protonic defects and dissolved oxygen is important. In the solid phase, the composition of adsorbed species on the catalyst layer surface will determine reaction rates. Denote the molar concentration

of species k by U_k; then each species will satisfy a conservation law of the form

$$\partial_t U_k + v.\nabla U_k - \nabla \cdot (D_k(\psi)\nabla U_k) = \sum_{j=1}^{N_r} R_j(U,\psi)s_j^k, \tag{4.3}$$

where for each of the N_r reactions, R_k denotes the scalar reaction rate and s_j^k is the corresponding stoichiometric constant relating the impact of reaction j on species k. The reaction rates will also couple into the phase equation

$$\psi_t + v.\nabla\psi = -\gamma\mathcal{G}_\rho\frac{\delta\mathcal{A}}{\delta\psi} + \sum_{j=1}^{N_r} R_j(U,\psi)\vec{s}_j, \tag{4.4}$$

where the phase stoichiometric vector $\vec{s}_j \in \mathbf{R}^3$ relates the impact of reaction j on the phase vector. The reaction rates are supported on the regions where ψ lies close to the saddle connections between each pair of minima.

The principle reactions are the ORR, the conversion of liquid water to vapor, and the adsorption of liquid water into the ionomer. Since the accumulation of liquid water is one of the slowest processes in the catalyst layer, the species transport is quicker to relax to steady-state than the water driven expansion of the ionomer, or the build-up of liquid water within the agglomerates. The species transport is at steady-state with respect to the phase evolution; however, variation in forcing terms, such as in AC impedance studies [30, 38], requires inclusion of time variation. As well, mass transfer limitations, such as Henry's law, which relates the concentration of dissolved oxygen in liquid to the oxygen concentration in the gas phase, can be included as reaction terms which consume gas phase oxygen and produce dissolved oxygen with a rate proportional to the disequilibrium.

4.3. Catalyst layer degradation. Many of the operating conditions to which a PEM fuel cell is exposed in automotive applications can lead to degradation of the catalyst layer; see [12] for a comprehensive review. Some specific experimental work is described in [120, 121]. There are two main degradation mechanisms in catalyst layers of current concern: corrosion of carbon support particles at electrode high potentials and the dissolution and movement of Pt particles, which also occur at high potentials. Identifying operating conditions that lead to high electrode potentials, how high they are, and where they occur, can be done only by considering unit cell and possibly stack level effects, discussed in section 6.

Modeling which resolves the phase structure of the catalyst layer is essential to verifying hypotheses on mechanisms for corrosion, in particular, predicting where within the catalyst layer and under which operating conditions carbon corrosion events occur, and how these events are affected by nanostructure and liquid hydration. Similarly, Pt dissolution is sensitive to voltage and oxygen concentrations. Dissolution of Pt ions has been found to increase with hydrogen concentrations [122]. Understanding and verifying mechanisms for Pt dissolution requires the knowledge of the nanoscale phase structure.

4.3.1. Carbon corrosion. Carbon corrosion can be generated by short-term events, such as anode/cathode understoich for which the voltages of the anode and catalyst layers rise substantially relative to the standard hydrogen electrode (SHE) [89], or by long-term events, such as when a particular cell in a stack is driven at understoich because of liquid water blockage of flow fields. At high electrode potentials

(roughly greater than 0.8 volts at 65°C), carbon in the catalyst layers can be oxidized at a significant rate with the following reaction (c):

$$C. + 2H_2O \rightarrow CO_2 + 4H^+ + 4e^-. \tag{4.5}$$

The actual reaction path may be much more complex, possibly involving several intermediate surface oxides [44]. At high electrode potentials (roughly greater than 1.2V), reverse ORR (h) can also occur:

$$2H_2O \rightarrow O_2 + 4H^+ + 4e^-. \tag{4.6}$$

The electrode potential E varies with the local concentration of reactants and the local current density:

$$E = E_{r,\mathrm{ref}} + N(U) + \eta_s(i_s), \tag{4.7}$$

where $E_{r,\mathrm{ref}}$ is the reference potential for reaction r, N represents Nernst terms which depend upon the local molar concentration of reactants U, and η_s is the overpotential associated with reaction s. Typical values for reference potentials differ widely—$E_{h,\mathrm{ref}} = 0$ for hydrogen evolution, $E_{o,\mathrm{ref}} = 1.28V$ for oxygen reduction, and $E_{c,\mathrm{ref}} = 0.207V$ for carbon corrosion—so that cell voltage relative to SHE has a considerable impact on the three reaction rates. For each reaction ($s = o, h, c$) the overpotential relates the reaction rate (equivalent current) to the voltage through a Butler–Volmer relation:

$$i_s = i_{s,\mathrm{ref}} \left\{ \exp\left(\frac{\alpha_s \mathcal{F} \eta_s}{\mathcal{R}T} \right) - \exp\left(-\frac{(1-\alpha_s)\mathcal{F}\eta_s}{\mathcal{R}T} \right) \right\}. \tag{4.8}$$

The local reaction rate i_s for each reaction s couples strongly to the whole cell through the voltage balance relation (2.7). In previous modeling efforts [89, 118, 67], each of the three reactions (ORR, reverse ORR, carbon corrosion) competes to provide the local cell current, $i = i_o + i_h + i_c$, with oxidation reactions generating positive currents and reduction reactions negative currents. Unit cell models were coupled to macrohomogeneous catalyst layer models for the three competing reactions, which was able to predict regions of carbon corrosion arising from an anode understoich. Carbon lost in this way leads to a reduction in the number of available catalyst sites with a corresponding reduction of EPSA and reduced performance. In hydrogen starved regions, forward current is carried by these two mechanisms (4.5), (4.6), leading to anode degradation. High potential can also occur on the cathode during start-up [67] (see the discussion in section 6) and at steady-state at low current densities [118]. Current models cannot predict the change in performance that this degradation causes. To do so would require the inclusion of these addition reactions into nanostructured performance-type models which would permit a more detailed resolution of the impact of corrosion events on catalyst composition and on the overall mechanisms of catalyst layer degradation. However, quantitative accuracy may be difficult to achieve since the kinetic parameters for these reactions (for a realistic reaction path or even an overall average) are notoriously hard to determine experimentally.

4.3.2. Platinum migration. Two principle mechanisms for platinum loss in the catalyst layer have been proposed, surface migration and Pt dissolution/reprecipitation. Recent work, however, [89], suggests that Pt dissolution is the major source of Pt surface area loss. Moreover, it has been shown [122] that potential cycling can induce Pt dissolution, that the rates of dissolution are greatly impacted by molecular

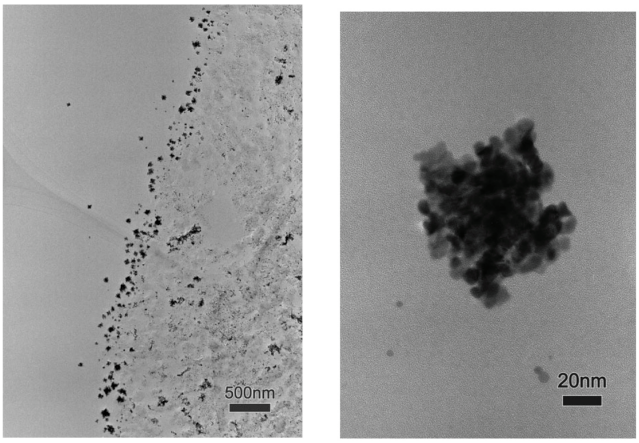

FIG. 4.2. *Images of Pt migration. Reprinted from* [*K. Yasuda, A. Taniguchi, T. Akita, T. Ioroi, and Z. Siroma,* Platinum dissolution and deposition in the polymer electrolyte membrane of a PEM fuel cell as studied by potential cycling*, Phys. Chem. Chem. Phys.,* 8 (2006)*, pp.* 746–752]. *Copyright* © 2006. *Reproduced by permission of the PCCP Owner Societies. All rights reserved. Left: A TEM image of the interface between the cathode catalyst layer and the polymer electrolyte membrane of an MEA after a potential cycling test for* 500 *cycles under a nitrogen atmosphere. Potential cycling range:* 0.1–1.2 *volts vs. SHE. Right: Enlargement of deposited Pt particles.*

hydrogen concentrations, and that the location of Pt deposits moves toward the anode with reduction of hydrogen concentration in the membrane. The authors propose that Pt dissolves at high potential and that the Pt which does not recombine onto carbon support diffuses out of the catalyst layer to be reduced by hydrogen within the membrane; see Figure 4.2.

Platinum migration caused by dissolution is a serious degradation issue and a major limitation to PEM fuel cell operational lifetime. Platinum that migrates in this way may no longer be available as an active catalyst site [12], reducing the EPSA and hence overall performance of the fuel cell. This phenomenon can also be investigated by assuming additional reactions in the catalyst layer beyond those considered in the detailed models above. Darling and Meyers [24, 25] developed models of platinum migration after dissolution. The authors considered both electrochemical and chemical (from platinum oxide) dissolution paths, which can be present in different conditions:

$$\begin{aligned} Pt &\rightarrow Pt^{2+} + 2e^-, \\ Pt + H_2O &\rightarrow PtO + 2H^+ + 2e^-, \\ PtO_2H^+ &\rightarrow Pt^{2+} + H_2O + e^-. \end{aligned} \tag{4.9}$$

These ODE type models are not detailed enough to determine the effect of different catalyst layer microstructures on the Pt migration phenomena. Modifying performance models to include the additional species Pt, PtO, and Pt ions, and the metallic Pt phase, both as attached to carbon substrate and as deposited particles, will permit an understanding of the impact of nanoscale geometry, hydration levels, hydrogen crossover, cathode voltage relative to SHE, and oxygen density on Pt dissolution, and highlight the operational conditions under which Pt dissolution is prominent. These models could be validated against potential sweep experiments and scanning electron micrographs (SEMs) of Pt deposits.

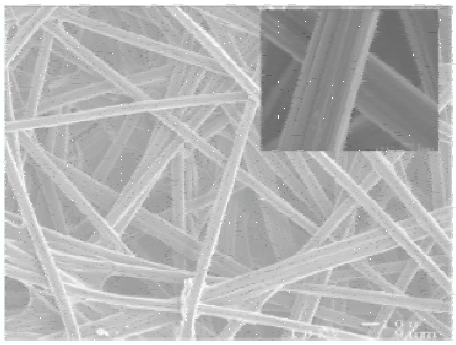

FIG. 5.1. *SEM micrographs of bare carbon paper. The inset is a high magnification image of the microfibers. Reprinted from* [*T. Bordjiba, M. Mohamedi, and L. H. Dao,* Binderless carbon nanotube/carbon fiber composites for electrochemical micropower sources*, Nanotechnology,* 18 (2007)*,* 035202].

5. Two-phase flow. Operating PEM fuel cells at conditions in which no liquid water forms generally leads to decreased performance due to higher membrane and catalyst layer ionomer protonic resistivity and shorter membrane lifetimes [12]. Thus, descriptive models of two-phase flow in the GDL and gas channels are needed. Experimental measurements of water in an operating cell are limited. Transparent cells can be used to observe water emerging from the cathode GDL and then moving in channels [100]. Nuclear magnetic resonance techniques hold some promise of resolving the water profiles within the MEA, but no well-resolved results are yet available. Estimates of the MEA water content can be obtained by weight comparison of pieces of the MEA taken out of a cell after operation [85]. Standard pore size distribution and characterization measurements [45] of GDL material are difficult due to the catalyst layer's small thickness. The GDL is often made of carbon fiber paper, which is a good conductor of electronic current and heat. It is known experimentally that teflonation of the GDL leads to improved water management. Changes in this hydrophobic treatment over time are another source of performance degradation [12]. However, the state of modeling is only approaching the stage where the performance of a given GDL structure can be characterized with computational models [93]. Some of the progress that has been made on two-phase flow in fuel cells is described below.

5.1. Two-phase GDL flow. We outline the framework for two-phase flow in porous media typically used in fuel cell models. After a brief discussion of one-phase flow we will concentrate on a simple model in which there is only liquid water and water vapor, ignoring the other gas species typical in fuel cell operation, such as hydrogen on the anode and oxygen and nitrogen on the cathode. The relative diffusion of these gaseous species is important and is often described using approximate Fickian terms [103] or more appropriate Stefan–Maxwell terms [26, 102]. These terms complicate the model, but do not make it mathematically more difficult.

5.1.1. One-phase flow. We consider the steady-state situation of vapor flowing in a GDL material. It is at pressure P and temperature T. The small pore size scale justifies taking the vapor and solid at thermal equilibrium (having the same local temperature); see Figure 5.1. We assume that the vapor obeys the ideal gas law, so

its density ρ is given by

$$\rho = \frac{M}{\mathcal{R}}\frac{P}{T}, \tag{5.1}$$

where M is the molar mass and $\mathcal{R}$ is the ideal gas constant. The average velocity $\mathbf{v}$ is related to pressure gradients through the standard empirical formula, Darcy's law:

$$\mathbf{v} = -\frac{\kappa}{\mu}\nabla P, \tag{5.2}$$

where κ is the permeability of the porous medium and μ is the viscosity of the gas. Conservation of mass and energy leads to

$$\nabla \cdot (\rho \mathbf{v}) = -\frac{M}{\mathcal{R}}\frac{\kappa}{\mu}\nabla \cdot \left(\frac{P}{T}\nabla P\right) = 0, \tag{5.3}$$

$$\nabla \cdot (-K\nabla T) = -K\Delta T = 0, \tag{5.4}$$

where K is the thermal conductivity of the solid. In (5.4) the thermal conductivity and the enthalpy of the gas are neglected. Equations (5.3), (5.4) are an elliptic system for P and T, and, although nonlinear, their numerical solution is straightforward.

The material parameters κ and K are not isotropic for GDL materials. However, successful programs have been carried out that take 3D scans of GDL materials and compute the anisotropic values of κ and K using ideas first developed to characterize the permeability of rocks in oil reservoirs [3]. Thus, it is possible to predict the behavior of new GDL materials in dry conditions without experimental testing in operating fuel cells. Some uncertainty remains due to how a given GDL material will behave when it experiences uneven compression (due to the alternating channel and rib areas of the plates) in a stack. The same level of prediction has not yet been achieved for how a GDL will behave in two-phase situations although some recent progress has been made [93]. Some of the issues are described below.

5.1.2. Two-phase GDL flow. Liquid water in the pores of a GDL can be described by a local average saturation s, the fraction of pore space filled with water ($0 \le s \le 1$). When $s = 0$, the one-phase gas equations of the section above are recovered. When $s > 0$ (the two-phase region), quite different equations apply as shown below. The two-phase boundary $s = 0$ is a free interface of the problem.

As justified in [86], within the two-phase region the vapor pressure can be taken equal to the saturation pressure:

$$P = P_{sat}(T), \tag{5.5}$$

where P_{sat} is an experimentally measured increasing function for which various fitted forms are available in the literature [16]. The time scale to reach this equilibrium has been shown to be several orders of magnitude larger than other time scales in GDL transport [86]. Including thermal effects is necessary when predicting two-phase flows in the GDL. There are strong thermal gradients in the GDL of an operating fuel cell that drive large vapor fluxes at saturation, and the accompanying condensation and evaporation generate pressure gradients which further drive the flow. The coupling of temperature and saturation is globally important in fuel cells, and capturing this global coupling to accurately describe water management in fuel cells is one of the major challenges in stack level modeling (see section 6).

With (5.5) giving the vapor pressure as a function of T, the two-phase zone is described by the variables s and T. We describe simple versions of equations for these variables below, introducing the condensation rate Γ. Vapor velocity is given by

$$\mathbf{v} = -\frac{\kappa\kappa_{rv}(s)}{\mu}\nabla P,$$

where the influence of the liquid water on vapor flow is encoded in the relative permeability $\kappa_{rv}(s)$, typically taken to be $1-s$ or $1-s^3$. The surface tension on the curved surface between liquid and vapor makes the liquid pressure P_l different from the vapor pressure P. It is assumed that this difference (the capillary pressure P_c) can be written as a function of s:

$$P_l = P - P_c(s).$$

In [55], Leverett made this ansatz and measured $P_c(s)$ (decreasing) for a certain type of hydrophilic sand. Later work led to predictions of how P_c should vary with porosity, permeability, and static contact angle. In many geophysical applications, the capillary pressure can be neglected, but in the small scales of a fuel cell GDL it can be a dominant term. The liquid pressure drives an average liquid water velocity $\mathbf{v}_l$ with a similar form to the vapor velocity above:

$$\mathbf{v}_l = -\frac{\kappa\kappa_{rl}(s)}{\mu_l}\nabla P_l,$$

where κ_{rl} is typically taken to be s or s^3. Conservation of liquid and vapor leads to the following equations:

$$\nabla\cdot(\rho\mathbf{v}) = -\Gamma,$$

$$\nabla\cdot(\rho_l\mathbf{v}_l) = \Gamma,$$

where the liquid water density ρ_l can be taken to be constant. These can be combined to give

$$\nabla\cdot(\rho\mathbf{v}+\rho_l\mathbf{v}_l) = 0, \tag{5.6}$$

which represents conservation of total water. The condensation is a large heat source:

$$-K\Delta T = h_{vap}\Gamma = -h_{vap}\nabla\cdot(\rho\mathbf{v}), \tag{5.7}$$

where h_{vap} is the latent heat of vaporization. Equations (5.6), (5.7) represent an elliptic system for s and T, which can be seen more clearly in the following forms:

$$\begin{aligned} 0 = &-\frac{\kappa M}{\mu\mathcal{R}}\nabla\cdot\left(\frac{P_{sat}(T)\kappa_{rv}(s)}{T}\nabla P_{sat}(T)\right) \\ &-\frac{\kappa\rho_l}{\mu_l}\nabla\cdot\left(\kappa_{rl}(s)\nabla(P_{sat}(T)-P_c(s))\right), \end{aligned} \tag{5.8}$$

$$0 = -K\Delta T - \frac{h_{vap}\kappa M}{\mu\mathcal{R}}\nabla\cdot\left(\frac{P_{sat}(T)\kappa_{rv}(s)}{T}\nabla P_{sat}(T)\right). \tag{5.9}$$

At the two-phase zone interface (see the "mixed" region of Figure 5.2), five conditions are given: $s=0$, T is continuous, P is continuous and has the value $P_{sat}(T)$, mass flux

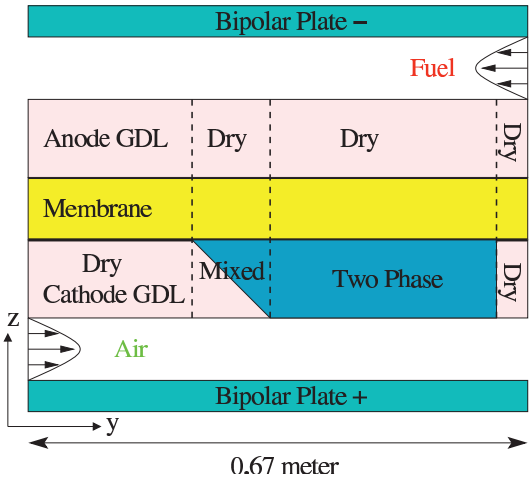

FIG. 5.2. *Depiction of typical single-phase, two-phase, and mixed regions in a fuel cell MEA and flow-field channel. Reprinted from* [*K. Promislow, P. Chang, H. Haas, and B. Wetton,* A two-phase unit cell model for slow transients in polymer electrolyte membrane fuel cells*, J. Electrochem. Soc.,* 155 (2008)*, pp.* A494–A504]. *Copyright* © 2008. *Reproduced by permission of The Electrochemical Society. All rights reserved.*

is continuous, and the thermal flux is continuous (taking into account the evaporation front at the interface). This interesting free boundary value problem has received little mathematical attention. A simple asymptotic description of the region near the two-phase zone boundary is given in [13]. The main difficulty is that the ellipticity in saturation is degenerate at the interface. Considering the system (5.8), (5.9), the only second-order term for s is

$$\frac{\kappa\rho_l}{\mu_l} P_c'(s)\kappa_{rl}(s)\Delta s.$$

The forms for $\kappa_{rl}(s)$ have $\kappa_{rl}(0) = 0$, leading to the degeneracy. The degeneracy leads to a singularity in the saturation at the two-phase zone interface [13].

A system like (5.8), (5.9) underlies most of the models of two-phase GDL flow in the literature. Some particular formulations and numerical approaches are discussed below. As discussed above, adding additional gas components makes the model more complex but does not add mathematical difficulty.

5.1.3. Computational formulations. In the models of sections 5.1.1 and 5.1.2 a fundamental difficulty is the elliptic degeneracy at the two-phase zone boundary. In time-dependent problems this is a parabolic degeneracy, and the two-phase zone interface velocity can only be written in a limiting form [14] similar to simpler degenerate problems [31]. This makes direct interface tracking [21] or level set methods [48] difficult to apply to the problem, since they rely on an expression for the normal velocity of the interface. Because of this, capturing methods [21] are attractive. These methods also fit more easily as components in the larger-scale simulations described in section 6. A formulation of the two-phase problem suitable for a capturing method must deal with the fact that the natural variables in the two-phase zone are different from those in the dry zone. A nice idea first formulated in [106] is to replace the saturation in the two-phase zone and the vapor pressure in the dry zone by the total

water density $\wp$:

$$\wp = s\rho_l + (1-s)\rho. \tag{5.10}$$

In both regions, the variables $\wp$ and T can be used. The vapor pressure P is recovered by the so-called M_2 map

$$P = \min\left(P_{sat}(T), \frac{\wp \mathcal{R} T}{M}\right).$$

The vapor pressure and T determine the vapor density ρ, and thus the saturation s can be recovered from (5.10). Capturing methods for two-phase transport in fuel cell GDL regions have been developed based on this idea [108] and incorporated into larger simulations. A version of this method has been shown to converge numerically to traveling wave solutions of model problems [14]. Because of the practical implementation and convergence verification, the authors consider this technique to be the current state of the art for this problem. However, no rigorous mathematical work has yet been done.

Other approaches to capturing methods have also been taken. The condition (5.5) can be relaxed, allowing P to be an independent variable in the two-phase zone. The condensation rate Γ is taken to be determined by the degree of oversaturation:

$$\Gamma = H(P - P_{sat}),$$

where the condensation rate H is taken to be large, although smaller than the physical value. In this way, a problem for s, P, and T over the whole domain is created. A cutoff to the evaporation rate when $s = 0$ must be added. This approach has been applied to fuel cell problems [9]. In addition, the elliptic degeneracy is removed in some calculations by taking $\kappa_{rl}(s) = s^3 + \epsilon$. Both of these approaches can be considered regularizations of the original problem. The convergence and its rate of the solutions in regularization parameters $\epsilon \to 0$ and $H \to \infty$ are open problems.

5.1.4. Other models. In [86] the authors considered a model in the framework above but with a large immobile water saturation level and an asymptotically large capillary pressure. The asymptotic problem leads to a simple description of GDL transport in which the singularity at the two-phase interface is no longer present. Computations based on a one-dimensional (1D) version of this model have been shown to match experimental results well [85] (see Figure 6.2).

All the models above rely on the assumption that two-phase flow can be described macroscopically by the correlations $\kappa_{rl}(s)$, $\kappa_{rv}(s)$, and $P_c(s)$. There are rigorous results showing that Darcy's law (5.2) is the correct macroscopic description of one-phase porous media flow (see [33] and the references therein for the original theory), but there is no such theoretical backing for the two-phase flow equations above. In fact, there is hysteresis in experimental results that show that physical systems cannot be described exactly in this way. In addition, there has been no progress in characterizing macroscopic two-phase flow from a given GDL microstructure that includes the level of teflonation. Some GDL materials have been shown to have two types of pores, teflonated ones that are hydrophobic and unteflonated ones that are hydrophilic. Clearly, flow in these two types of pores would have to be described differently. An alternate path for investigating two-phase flow in GDL regions is the pore network model [61].

5.2. Two-phase channel flow. The transport of heat, mass, and charge outside the MEA can be described by standard models with the notable exception of two-phase flow in gas channels. Macroscopically what is needed is a description of the average local channel pressure drop as a function of given local gas and liquid water fluxes. Standard models of two-phase flow [34] do not apply since they neglect capillary (surface tension) effects that are large at the length scales of fuel cell channels. A reasonable model would have to take into account the surface characteristics of the channel walls and the GDL, which experimental testing has shown to be important. Several groups are working on experimentally determining such a correlation. Visualization using transparent cells shows that droplets of water emerge from the cathode GDL, are blown downstream, and coalesce [100]. Experiments on the anode side suggest that there is water condensation on the channel walls [36].

Some computational modeling of this phenomenon is currently being done. Such simulations require a description of dynamic contact angles of droplets, which is not physically well understood (see the discussion in [96]). As a whole, channel two-phase flow in fuel cells is not well understood. Particularly important is an understanding of the way water leaves the GDL and enters the channel. This would lead to an appropriate boundary condition for the saturation in the two-phase GDL problems described above. Currently, somewhat arbitrary Signorini conditions (equivalent to a Robin condition for the saturation) are often used as are homogeneous Dirichlet conditions for saturation [9].

6. Unit cell and stack level models. In sections 3, 4, and 5, *component models* for various parts of the MEA were discussed. These models and corresponding simulations can lead to better understanding of the processes in these components and hence to better designs. There is also interest in the simulation of complete unit cells and stacks. An important outcome of the studies on component models described above is the derivation of appropriate macroscopic descriptions of these components that can be used in these large simulations. The goal is to have a fast and accurate simulation tool of fuel cell stacks that can be used for a variety of purposes: optimization of designs and operating conditions using a given MEA with known properties, identification of failure modes and development of mitigation strategies, investigation of component tolerances, and investigation of new MEA designs and their impact on the global stack environment. Some examples of stack level phenomena of interest are given in section 6.1.

As mentioned above, most of the phenomena outside the MEA can be described by standard models of mass and thermal transport, with the exception of the two-phase flow in channels and the mechanism of liquid water entry into the channels from the GDL, as discussed in section 5.2. One approach to unit cell level simulation is based on *computational fluid dynamics (CFD) models*, usually full 3D CFD models with added modules for fuel cell specific components (e.g., [64, 65, 70, 74, 79]). Major simplifications are usually made to the MEA component models. Even with these simplifications, these models are very computationally intensive even for single cell/single channel computations, and the resolution in the channel cross-plane (see Figure 2.2) is usually quite coarse. The CFD-based approach is capable of predicting performance including geometrical changes to plates; however, stack level CFD simulations or fuel cell simulations within an optimization process are not currently practical. Significant speed-up in fuel cell CFD computations is needed in order for them to contribute to the design process.

Lower dimensional, *averaged models* are an alternative to CFD-based modeling

that nevertheless include much of the complex coupling of phenomena found in fuel cells [18, 35]. These models consider transport through the MEA as 1D processes (averaged over the cross-channel direction) coupled to 1D models of channel and coolant flow. Thus, they are also known as "1+1D" models. Reduced dimensional models can be simulated rapidly, even at the stack level. However, they necessarily lack the accurate description of the cross-channel geometry, which is averaged over and replaced by fitted transport coefficients. Fundamentally changing this geometry requires a refitting of these coefficients based on additional experimental measurements. These averaged models can be fit to existing stack designs and give some insight into behavior of these stacks. However, it is not clear how much they can contribute to the design process.

Large scale CFD simulation of fuel cells has been taken up by several large engineering groups, such as the groups at Penn State (led by C. Y. Wang), University of South Carolina (J. Van Zee), and the University of Victoria (N. Djilali). Reduced dimensional models lead to smaller scale problems which are more tractable for numerical investigation. Morever, improvements in solution strategy derived for these reduced models can lead to improvements in CFD codes. Identifying which reductions do not reduce accuracy (analytically or by comparison to benchmark problems as discussed in section 6.5) would be an important contribution to the field. A simple example of a 1+1D unit cell model is given in section 6.2, with a discussion of the extensions made in state-of-the-art models of this type for unit cells and stacks.

6.1. Some examples of stack level phenomena. At a given channel location within a single cell, local reaction and transport, thermal and electrical coupling between cells through shared bipolar plates, end plate effects, and flow sharing effects through gas and coolant headers can all be important. In some cases, questions about local behavior can be answered only by also considering stack level effects. Three examples of multiscale phenomena in fuel cells are given below. There are many others.

Low end cells. Cells at the ends of the stack (end cells) can lose significant amounts of heat to their environment. These cells operate at lower temperatures than interior cells. The lower temperature means there is more liquid water in the gas channels. This extra liquid water impedes the flow of reactant gases which are delivered by headers shared by all cells. If the effect is severe enough, the amount of flow to the cell may be less than required (understoich), leading to cell failure. This scenario can be modeled only by considering unit cell gas channel flow and reaction combined with stack level thermal and header effects. The end cell may also introduce significant electrical coupling effects with other cells by its anomalous performance.

Cell start-up. A cell that is shut down will eventually come into equilibrium with ambient air. When the cell is restarted, hydrogen is introduced into the anode. During this transient, a condition exists where the anode is hydrogen rich at inlet but has ambient air at outlet. The conditions at inlet (corresponding to regular fuel cell operation) drive the cell voltage positive. A recirculation current is formed, with positive current at anode inlet and negative current at anode outlet. The negative current on the cathode side consists of reverse ORR and also carbon oxidation. This latter reaction is one of the major lifetime limiting factors in current designs as discussed in section 4.3.1. To understand this process, models that couple channel flow to electric potential at the cell level are needed [67]. In the automotive application, additional issues arise when starting up a stack from subzero temperatures [12].

Stack compression. Stacks of cells are bolted together with large compression. This is done to maintain gas seals: it is an important safety concern to keep pressurized hydrogen from escaping from fuel cells. The stack compression is also needed to maintain good electrical and thermal contact between the MEA and the plates. It is well known that the level of compression of the membrane greatly affects its water uptake [4, 71] and so its conductivity. The coupling of compression to performance is known to cause complex behavior in model experimental systems [4]. Models considering these effects at a stack level have not yet been considered in the literature.

6.2. 1+1D unit cell models. We present here the *simplest* reduced dimensional unit cell model of the type in the literature [35, 7, 112, 123], following closely the discussion in [5]. The simplifications in the model include that the cathode gas channels are assumed saturated along their entire length and that the anode is run at a reasonably high hydrogen stoich. We neglect water crossover between the anode and the cathode and assume that the cell is run at isothermal conditions. Under these assumptions the membrane electrical resistivity R can be assumed to be constant along the channel. The influence of the anode channels on cell performance is negligible, and thus the anode flow can be removed from the computation. Pressure drop along the cathode channel is neglected.

This simple unit cell model involves the determination of the cell voltage V (taken to be constant along the length of the cell), the current density $i(x)$, and the oxygen flux $Q_o(x)$ and oxygen concentration $C_o(x)$ profiles. As a reminder, x is the coordinate of the channel from $x = 0$ (cathode inlet) to $x = L_c$ (cathode outlet). All quantities are averaged over the channel cross-plane (y-z), giving the dimensional reduction. An ideal control parameter is the dimensionless cathode stoichiometric flow rate $s > 1$ which determines the cathode inlet oxygen flux (per unit width in z), $Q_o(0) = si_dL_c/(4\mathcal{F})$, and the cathode inlet nitrogen flux, $Q_n(0) = Q_o(0)(0.79)/(0.21)$, where i_d is the given target average current density and $(0.79)/(0.21)$ appears as the assumed ratio of nitrogen to oxygen in the inlet stream. Other trace gases in air are neglected.

A mass balance relates the flux of oxygen to the current density via Faraday's constant, $\mathcal{F}$:

$$\frac{dQ_o}{dx} = \frac{i(x)}{4\mathcal{F}}. \tag{6.1}$$

Using the ideal gas law, the fact that the nitrogen is unreactive and thus its flux is constant from inlet to outlet, an assumption that oversaturated vapor immediately condenses, and that all gaseous species are transported by channel convection only with a common average velocity, we obtain the algebraic relationship

$$C_o = \frac{(P_c - P_v)Q_o}{(Q_o + Q_n)\mathcal{R}T} \tag{6.2}$$

between $Q_o(x)$ and $C_o(x)$. Here, P_c is the pressure in the cathode channels (taken to be constant), and P_v is the vapor partial pressure at temperature T. See [7] for details.

We use the Butler–Volmer relationship below with cell voltage V to be determined and fitted parameters R, α_c, C_{ref}, δ, and i_{ref} given in [5]:

$$V = E_0 - iR - \frac{\mathcal{R}T}{\mathcal{F}\alpha_c} \ln \frac{iC_{\text{ref}}}{i_0(C_o - \delta i)}. \tag{6.3}$$

This is (2.7), neglecting anode losses (2.6) with an approximation of (2.5) for large current densities i. Here, $C_o - \delta i$ approximates the oxygen concentration at catalyst sites, lower than the channel average because the oxygen must diffuse through the GDL and catalyst layer to the active sites. The concentration reduction should be proportional to the flux, which is proportional to the local current, leading to the given form. The parameter δ can be related to an effective diffusivity, but many processes are lumped into this parameter, including concentration losses from diffusion from channel average to GDL boundary, diffusion through the porous GDL, and diffusion of dissolved oxygen through the ionomer in the catalyst layer. The most distinguished feature of δ is that it specifies the maximum current, $i_{\max} = C_o/\delta$, that can be drawn at fixed oxygen concentration. In implementation the singularity in (6.3) at $i = i_{\max}$ is relaxed to allow currents larger than this maximum in iterative computations (see [5] for details).

Equations (6.1), (6.2), and (6.3) with the inlet fluxes given above and the requirement that the cell draws the given average current density,

$$\frac{1}{L_c}\int_0^{L_c} i(x)dx = i_d, \tag{6.4}$$

completely specify the unit cell model. Motivated by the stack level models described below, we consider $i(x)$ to be the fundamental variable of the problem. For a given $i(x)$, (6.1) can be integrated to give $Q_o(x)$, (6.2) gives $C_o(x)$, and then (6.3) gives $V(x)$. Thus, $V(\cdot)$ is determined nonlocally by $i(\cdot)$, denoted by $V[i]$. The solution $i(x)$ makes the resulting V constant in x, which can be expressed as

$$\frac{d^2V[i]}{dx^2} = 0 \qquad \text{with} \frac{dV[i]}{dx}(0) = \frac{dV[i]}{dx}(L_c) = 0 \tag{6.5}$$

with additional condition (6.4). It can be shown [18] (in a simple, linear setting) that approximate Newton's iterations (using only the local dependence of V on i) of (6.5) converge for a large parameter range of physical interest at a grid-independent rate. This has been confirmed in many computational studies.

Computational current densities for oxidant stoichiometric flow rates of 1.8 and 1.2 are shown in Figure 6.1, compared with experimental results from the Ballard Mk 9 architecture (the experiments are described in more detail in [7]). The agreement in current density profile is reasonable, and the cell voltages agree quite well.

Starting with this simple framework, much more realistic unit cell models can be specified. Even though the anode kinetics (2.6) can often be neglected, the anode gas stream is an important aspect of *water management* due to water crossover through the membrane. Since channel gases are not always saturated, water vapor fluxes and concentrations can be added to the model. The resulting model has discontinuities at channel locations where the gas stream saturates that must be handled carefully [18, 85]. In the through-MEA direction y, membrane models of various complexity can be added, using fitted, average forms of the models described in section 3. These take into account water crossover between anode and cathode channel streams and the dependence of membrane resistivity on its water content. Thermal profiles in y can also be determined, taking into account the heat generated by reaction and the phase change of water. Simple 1D models of heat transport through the MEA and bipolar plates and into the coolant channels can be included. Some examples of these kinds of models are found in [35, 18, 123]. The extension to models that also include two-phase flow in the GDL is recent [112, 85]. The agreement of these models to GDL water content can be quite good, as shown in Figure 6.2.

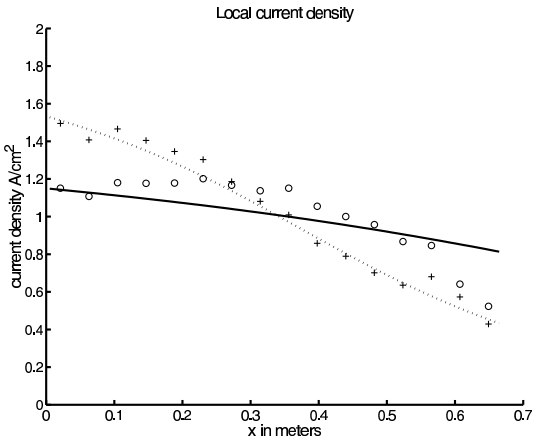

FIG. 6.1. *Comparison of experimental unit cell current density measurements with the model at two cathode stoichiometric flow rates: stoich* 1.8 *shown by solid line (model, voltage* 0.6450*) and circles (experiment, voltage* 0.6360*); stoich* 1.2 *shown by dotted line (model, voltage* 0.5904*) and pluses (experiment, voltage* 0.5969*).*

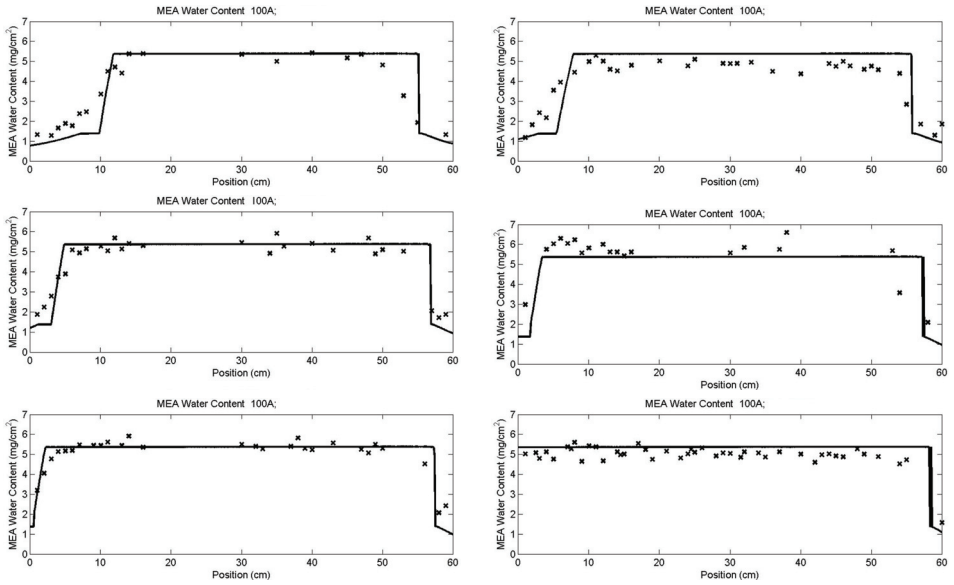

FIG. 6.2. *Comparison of computed MEA water contents (solid line) to experimental data (×) at* 0.33 *A/cm*^{2} *under counterflowing conditions. Reprinted from* [*K. Promislow, P. Chang, H. Haas, and B. Wetton,* A two-phase unit cell model for slow transients in polymer electrolyte membrane fuel cells*, J. Electrochem. Soc.,* 155 (2008)*, pp.* A494–A504]. *Copyright* © 2008. *Reproduced by permission of The Electrochemical Society. All rights reserved. The inlet coolant temperature is reduced between each experiment, starting at* 70° *C in the upper left followed left to right by* 65.5°*,* 64.5°*,* 63.5°*,* 62.5°*, and* 60.5° *C at the bottom right. The two-phase region expands toward the air inlet (left), but does not reach the outlet.*

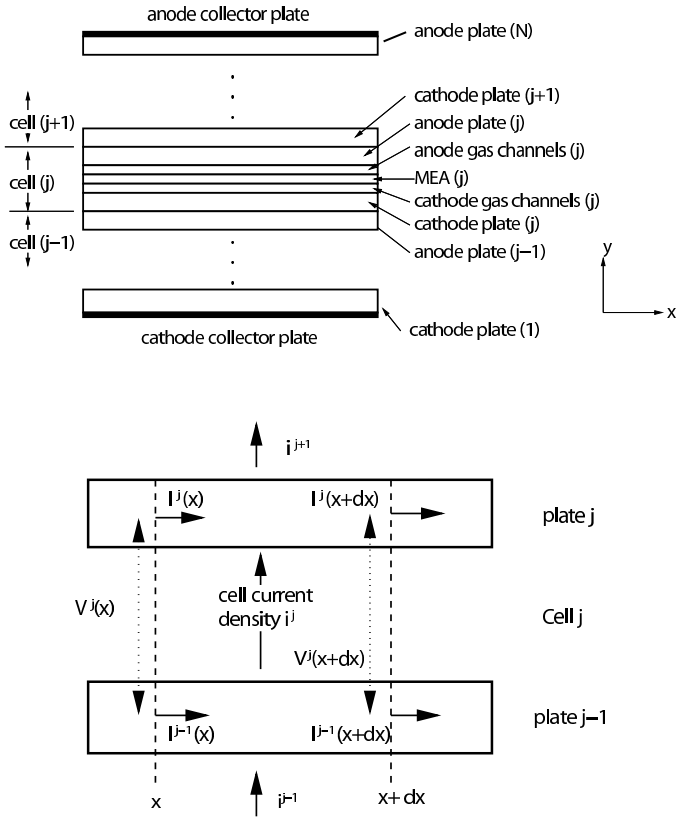

FIG. 6.3. *Top: A depiction of a unit cell stack showing the layering of bipolar plates, gas channels, and MEAs. The cells are coupled through thermal and electrical effects. Bottom: Diagram showing the derivation of* (6.6) *and* (6.7).

6.3. 1+1D stack level models. The 1+1D unit cell models can be extended to the stack environment. Considering a stack of N cells, indexed by a superscript j, the same total current flows through each cell, but the local current densities $i^j(x)$ can vary between cells. The difference in current densities between adjacent cells drives currents I^j (in the x direction, per unit width z) in the bipolar plates (the plate j is above cell j; see Figure 6.3 (top)). The plates have significant resistance to the plate currents, and so cell voltages can vary with position: $V^j = V^j(x)$.

As in the 1+1D unit cell model above, we consider the current densities $i^j(x)$ as the fundamental variables. These determine $V^j(x)$ through relationships like (6.3) in which the oxygen concentration, and possibly temperature, is determined nonlocally. The governing relationship for the voltages $V[i]$ is derived below. Considering Figure 6.3 (bottom), conservation of current in the length "dx" of plate j yields

$$\frac{dI^j}{dx} = i^{j+1}(x) - i^j(x), \tag{6.6}$$

where plate currents are given per unit orthogonal length and cell currents are given per unit area. The plate currents lead to voltage drops in the plates. The difference

in voltage between plate j and $j-1$ is $V^j(x)$; thus

$$\frac{dV^j}{dx} = \lambda(-I^j + I^{j-1}). \tag{6.7}$$

Here λ is a measure of plate resistance (resistance per unit length to plate currents per unit width). Differentiating (6.7) and using (6.6) the plate currents can be eliminated giving

$$\frac{d^2V^j}{dx^2} - \lambda(i^{j-1} - 2i^j + i^{j+1}) = 0, \tag{6.8}$$

which we named the *fundamental voltage equation*. Considering (6.3) we see that $V'(i) < 0$ (locally) giving (6.8) the character of a partially discretized nonlinear elliptic problem in nondivergence form. Boundary conditions for each cell are

$$\frac{dV^j}{dx}(0) = 0, \tag{6.9}$$

$$\frac{dV^j}{dx}(L_c) = 0. \tag{6.10}$$

These correspond to the conditions that the plate currents must be zero at inlet and outlet, as seen from (6.7). Additional conditions are given at end cells 1 and N at collector plates; see [5] for details. The problem (6.8)–(6.10) with (6.4) specified for one cell can be solved for i^j, $j = 1, \ldots, N$. Approximate Newton iterations using only the local sensitivity of V with i as described above for unit cell models are also effective in the stack setting.

Implementations of stack level models of this type are described in [18, 35], with experimental validation of the modeling of the effects of electrical coupling between cells reported in [49]. Asymptotic analysis estimating the extent, as measured by the number of affected adjacent cells, of anomalies has been done using these models for thermal [87] and electrical [5] coupling.

Several important aspects of fuel cell stacks remain to be added to such models. A parameterized effect of liquid water transport in channels remains to be added, but there are open questions on the modeling as discussed in section 5.2. Thermal end cell effects and flow sharing effects between cells from shared gas headers using simple flow network models like those proposed in [19, 47] could be added. Adding resolution in the cross-plane as discussed in the next section would also improve this approach.

6.4. Fuel cell cross-plane. Some attempts have been made to combine the advantages of CFD and averaged models. Currently, some CFD models are being developed in which the channel flow is reduced to a 1D average. Some authors (e.g., [105]) consider 2D models in the x-z plane of Figure 2.1 that are similar in spirit to the 1+1D models discussed above. The authors believe that the cross-plane problem (see Figure 2.2) is the fundamental building block for accurate unit cell and stack level simulation. This cross-plane problem can be considered as a 2D problem or as a 2D plus microstructure cell problem for more complex MEA models. Several authors consider pieces of this problem in 2D computations [69, 9, 108]. However, water management is a key issue that can be resolved only by understanding how water and heat flux is directed to the anode and cathode. This requires the consideration of all components in the cross-plane of Figure 2.2.

For given average current density, coolant temperature, and gas flux, the cross-plane problem can be made into a local problem. How to couple these local problems thermally and electrically and with header effects at the stack level to solve for consistent local average values is well understood for 1+1D models [18]. Extending these ideas to 2+1D models in the cross-plane discussed above should be possible. The authors believe that this framework will provide the optimal trade-off between model accuracy and computational tractability for fuel cell simulation. This framework focuses attention on the difficult cross-plane computation that can be considered as a building block for multiple channel, multiple cell stack simulation. A preliminary version of this idea is given in [52] using a simplified cross-plane problem.

6.5. Benchmark problems. In many applications where computational models are now an integral part of the design process, there are well established computational benchmark problems to assess the accuracy and speed of new methods. An historical example is the driven cavity problem for 2D incompressible flow [37]. More modern examples are the benchmark problems for aeronautical flows and high performance computing [27].

The fuel cell application so far lacks such benchmark problems with highly accurate numerical solutions computed with methods with some theoretical backing. There are several reasons for the lack of such benchmarks. There is a lack of consensus on appropriate component models for the MEA (membrane, catalyst layer and GDL transport) and so comparison to experimental results has been seen to be much more important than assessing numerical accuracy. In addition, MEA design has changed rapidly using empirical reasoning so there is no "fixed target" for benchmark problems.

However, fuel cell simulation has recently reached the level of maturation at which benchmark problems should be introduced. Considerable effort is being put into large-scale, parallel computations of fuel cell models. It makes sense to have a rigorous way of assessing the performance of these calculations. The ingredients for an appropriate benchmark problem include detailed models of the MEA components with thermal coupling to coolant channels. Some consensus on the component models should be reached with input from the engineering community. The problem should be rigorously posed mathematically but in a form that is implementable in the frameworks already developed by major groups. Accurate solutions should be computed with an academic code that has some theoretical backing (ideally, proved convergent). A family of problems based on the cross-plane discussed in section 6.4 might form a suitable framework for highly resolved numerical solutions to a benchmark problem.

7. Conclusion. The transition to a carbon-lite energy infrastructure will require the efficient conversion of energy, particularly between high-density chemical forms and electric potential. Catalytic systems capable of achieving efficient energy conversion require high densities of reactive surface area and hence small length scales. Moreover, they require networks with selective transport properties to feed reactants to the catalyst sites. The modeling and analysis of these network driven composites and their construction, performance, and degradation will require the development of new mathematical structures and the quantization of deep connections between subscale models and continuum mechanics. PEM fuel cells are prime examples of energy conversion systems, and as such they possess functional structure from the nanoscale up to the macroscale. Their descriptive models are inherently multiscale and multiphysics. The computational realization of these models leads to stiff systems with widely varying length and time scales. With proper analysis, in some

scaling regimes, these systems can be reduced to lower dimensional ones that are better conditioned. However, for resolution of the relevant material science and device performance questions, highly structured, highly adaptive numerical methods will necessarily be required. Mathematical analysis and scientific computation will play a large role in the resolution of these important issues.

Acknowledgments. We would like to thank Peter Berg, Radu Bradean, Atife Caglar, Paul Chang, Nedjib Djilali, John Kenna, Gwang-Soo Kim, Shanna Knights, Michael Lauritzen, Herwig Haas, Arian Novruzi, Jean St-Pierre, John Stockie, Jürgen Stumper, and Jay Sui for valuable discussions of fuel cell operation and modeling over the years.

REFERENCES

[1] N. Alikakos, P. Bates, and X. Chen, *Convergence of the Cahn-Hilliard equation to the Hele-Shaw model*, Arch. Rational Mech. Anal., 128 (1994), pp. 165–205.

[2] N. D. Alikakos, S. I. Betelu, and X. Chen, *Explicit stationary solutions in multiple well dynamics and nonuniqueness of interfacial energy densities*, European J. Appl. Math., 17 (2006), pp. 525–556.

[3] A. S. Al-Kharusi and M. J. Blunt, *Network extraction from sandstone and carbonate pore space images*, J. Petrol. Sci. Eng., 56 (2007), pp. 219–231.

[4] J. Benziger, *The dynamic response of PEM fuel cells to changes in load*, Chem. Eng. Sci., 60 (2005), pp. 1743–1759.

[5] P. Berg, A. Caglar, J. St-Pierre, K. Promislow, and B. Wetton, *Electrical coupling in proton exchange membrane fuel cell stacks: Mathematical and computational modelling*, IMA J. Appl. Math., 71 (2006), pp. 241–261.

[6] P. Berg, A. Novruzi, and K. Promislow, *Analysis of a dry 1D cathode catalyst layer model for a polymer electrolyte fuel cell*, Chem. Eng. Sci., 61 (2006), pp. 4316–4331.

[7] P. Berg, K. Promislow, J. St-Pierre, J. Stumper, and B. Wetton, *Water management in PEM fuel cells*, J. Electrochem. Soc., 151 (2004), pp. A341–A353.

[8] T. Berning, D. Lu, and N. Djilali, *Three-dimensional computational analysis of transport phenomena in a PEM fuel cell—a parametric study*, J. Power Sources, 124 (2003), pp. 440–452.

[9] E. Birgersson, M. Noponen, and M. Vynnycky, *Analysis of a two-phase nonisothermal model for a PEFC*, J. Electrochem. Soc., 152 (2005), pp. A1021–A1034.

[10] L. Borcea and G. C. Papanicolaou, *Network approximations for transport properties of high contrast materials*, SIAM J. Appl. Math., 58 (1998), pp. 501–539.

[11] T. Bordjiba, M. Mohamedi, and L. H. Dao, *Binderless carbon nanotube/carbon fiber composites for electrochemical micropower sources*, Nanotechnology, 18 (2007), p. 035202.

[12] R. Borup, J. Meyers, B. Pivovar, Y. S. Kim, R. Mukundan, N. Garland, D. Myers, M. Wilson, F. Garzon, D. Wood, P. Zelenay, K. More, K. Stroh, T. Zawodzinski, J. Boncella, J. E. McGrath, M. Inaba, K. Miyatake, M. Hori, K. Ota, Z. Ogumi, S. Miyata, A. Nishikata, Z. Siroma, Y. Uchimoto, K. Yasuda, K.-I. Kimijima, and N. Iwashita, *Scientific aspects of polymer electrolyte fuel cell durability and degradation*, Chem. Rev., 107 (2007), pp. 3904–3951.

[13] L. Bridge, R. Bradean, M. J. Ward, and B. R. Wetton, *The analysis of a two-phase zone with condensation in a porous medium*, J. Engrg. Math., 45 (2003), pp. 247–268.

[14] L. Bridge and B. R. Wetton, *A mixture formulation for numerical capturing of a two-phase/vapor interface in a porous medium*, J. Comput. Phys., 225 (2007), pp. 2043–2068.

[15] K. Broka and P. Ekdunge, *Modeling the PEM fuel cell cathode*, J. Appl. Electrochem., 27 (1997), pp. 281–289.

[16] A. L. Buck, *New equations for computing vapor pressure and enhancement factor*, J. Appl. Meteorol., 20 (1981), pp. 1527–1532.

[17] J. W. Cahn, *On spinodal decomposition*, Acta Metall., 9 (1961), pp. 795–801.

[18] P. Chang, G. S. Kim, K. Promislow, and B. R. Wetton, *Reduced dimensional models of polymer electrolyte membrane fuel cell stacks*, J. Comput. Phys., 223 (2007), pp. 797–821.

[19] P. Chang, J. St-Pierre, J. Stumper, and B. Wetton, *Flow distribution in proton exchange membrane fuel cell stacks*, J. Power Sources, 162 (2006), pp. 340–355.

[20] P. Choi, N. H. Jalani, and R. Datta, *Thermodynamics and proton transport in Nafion. I. Membrane swelling, sorption, and ion-exchange equilibrium*, J. Electrochem. Soc., 152 (2005), pp. E83–E89.

[21] J. Crank, *Free and Moving Boundary Problems*, The Clarendon Press, Oxford University Press, New York, 1984.
[22] M. B. Cutlip, *An approximate model for mass transfer with reaction in porous gas diffusion electrodes*, Electrochim. Acta, 20 (1975), p. 767.
[23] K. Damen, M. van Troost, A. Faaij, and W. Turkenburg, *A comparison of electricity and hydrogen production systems with CO2 capture and storage. Part* A: *Review and selection of promising conversion and capture technologies*, Progr. Energy Combust. Sci., 32 (2006), pp. 215–246.
[24] R. M. Darling and J. P. Meyers, *Kinetic model of platinum dissolution in PEMFCs*, J. Electrochem. Soc., 150 (2003), pp. A1523–A1527.
[25] R. M. Darling and J. P. Meyers, *Mathematical model of platinum movement in PEM fuel cells*, J. Electrochem. Soc., 152 (2005), pp. A242–A247.
[26] J. Divisek, J. Fuhrmann, K. Gärtner, and R. Junga, *Performance modelling of a direct methanol fuel cell*, J. Electrochem. Soc., 150 (2003), pp. A811–A825.
[27] J. Dongarra and P. Luszczek, *Introduction to the HPC Challenge Benchmark Suite*, Technical report UT-CS-05-544, Computer Science Department, University of Tennessee, Knoxville, TN, 2005; available online at http://icl.cs.utk.edu/hpcc/.
[28] Q. Du, C. Liu, and X. Wang, *Simulating the deformation of vesicle membranes under elastic bending energy in three dimensions*, J. Comput. Phys., 212 (2006), pp. 757–777.
[29] M. Eikerling and A. A. Kornyshev, *Modelling the performance of the cathode catalyst layer of polymer electrolyte fuel cells*, J. Electroanal. Chem., 453 (1998), pp. 89–106.
[30] M. Eikerling and A. A. Kornyshev, *Electrochemical impedance of the cathode catalyst layer in polymer electrolyte fuel cells*, J. Electroanal. Chem., 475 (1999), pp. 107–123.
[31] S. Evje and K. H. Karlsen, *Monotone difference approximations of BV solutions to degenerate convection-diffusion equations*, SIAM J. Numer. Anal., 37 (2000), pp. 1838–1860.
[32] J. D. Fehribach, *Diffusion-reaction-conduction processes in porous electrodes: The electrolyte wedge problem*, European J. Appl. Math., 12 (2001), pp. 77–96.
[33] M. Firdaouss, J. L. Guermond, and P. LeQuere, *Nonlinear corrections to Darcy's law at low Reynolds numbers*, J. Fluid Mech., 343 (1997), pp. 331–350.
[34] A. C. Fowler, *Mathematical Models in the Applied Sciences*, Cambridge Texts Appl. Math., Cambridge University Press, Cambridge, UK, 1997.
[35] S. A. Freunberger, M. Santis, I. N. Schneider, A. Wokaun, and F. N. Buechi, *In-plane effects in large-scale PEMFCs: Model formulation and validation*, J. Electrochem. Soc., 153 (2006), pp. A396–A405.
[36] S. Ge and C.-Y. Wang, *Liquid water formation and transport in the PEFC anode*, J. Electrochem. Soc., 154 (2007), pp. B998–B1005.
[37] U. Ghia, K. N. Ghia, and C. T. Shin, *High-Re solutions for incompressible flow using the Navier-Stokes equations and a multigrid method*, J. Comput. Phys., 48 (1982), pp. 387–411.
[38] Q. Guo and R. White, *A steady-state impedance model for a PEMFC cathode*, J. Electrochem. Soc., 151 (2004), pp. E133–E149.
[39] L. G. Hector, Y.-H. Lai, W. Tong, and M. J. Lukitsch, *Strain accumulation in polymer electrolyte membrane and membrane electrode assembly materials during a single hydration/dehydration cycle*, J. Fuel Cell Sci. Tech., 4 (2007), pp. 19–28.
[40] J. T. Hinatsu, M. Mizuhata, and H. Takenaka, *Water uptake of perfluorosulfonic acid membranes from liquid water and water vapor*, J. Electrochem. Soc., 141 (1994), pp. 1493–1498.
[41] W. Y. Hsu and T. D. Gierke, *Ion transport and clustering in Nafion perfluorinated membranes*, J. Membrane Sci., 13 (1983), pp. 307–326.
[42] F. Jaouen, G. Lindgergh, and G. Sundholm, *Investigation of mass-transport limitations in the solid polymer fuel cell electrode:* I. *Mathematical model*, J. Electrochem. Soc., 149 (2002), pp. A437–A447.
[43] S. Kakac, A. Pramuanjaroenkij, and X. Y. Zhou, *A review of numerical modeling of solid oxide fuel cells*, Int. J. Hydrogen Energy, 32 (2007), pp. 761–786.
[44] K. H. Kangasniemi, D. A. Condit, and T. D. Jarvi, *Characterization of Vulcan electrochemically oxidized under simulated PEM fuel cell conditions*, J. Electrochem. Soc., 151 (2004), pp. E125–E132.
[45] A. M. Kannan and L. Munukutla, *Carbon nano-chain and carbon nano-fibers based gas diffusion layers for proton exchange membrane fuel cells*, J. Power Sources, 167 (2007), pp. 330–335.
[46] I. K. Kapdan and F. Kargi, *Bio-hydrogen production from waste materials*, Enzyme Microb. Technol., 38 (2006), pp. 569–582.
[47] G. Karimi, J. J. Baschuk, and X. Li, *Performance analysis and optimization of PEM fuel cell stacks using flow network approach*, J. Power Sources, 147 (2005), pp. 162–177.

[48] K. H. Karlsen, K.-A. Lie, and N. H. Risebro, *A fast marching method for reservoir simulation*, Comput. Geosci., 4 (2000), pp. 185–206.
[49] G.-S. Kim, J. St-Pierre, K. Promislow, and B. Wetton, *Electrical coupling in PEMFC stacks*, J. Power Sources, 152 (2005), pp. 210–217.
[50] K.-D. Kreuer, S. J. Paddison, E. Spohr, and M. Schuster, *Transport in proton conductors for fuel-cell applications: Simulations, elementary reactions, and phenomenology*, Chem. Rev., 104 (2004), pp. 4637–4678.
[51] K. D. Kreuer, M. Schuster, B. Obliers, O. Diat, U. Traub, A. Fuchs, U. Klock, S. J. Paddison, and J. Maier, *Short-side-chain proton conducting perfluorosulfonic acid ionomers: Why they perform better in PEM fuel cells*, J. Power Sources, 178 (2008), pp. 499–509.
[52] A. A. Kulikovsky, *Two models of a PEFC: Semi-analytical vs. numerical*, Int. J. Energy Res., 29 (2005), pp. 1153–1165.
[53] Y.-H. Lai, C. Mittelsteadt, C. Gittleman, and D. Dillard, *Viscoelastic stress model and mechanical characterization of perfluorosulfonic acid (PFSA) polymer electrolyte membranes*, FUELCELL 2005-74120, in Proceedings of the Third International Conference on Fuel Cell Science, Engineering and Technology, Ypsilanti, MI, 2005, ASME, New York, 2005.
[54] M. J. Lampinen and M. Famino, *Analysis of free energy and entropy changes for half-cell reactions*, J. Electrochem. Soc., 140 (1993), pp. 3537–3546.
[55] M. C. Leverett, *Capillary behavior in porous solids*, Trans. AIME, 142 (1941), pp. 152–169.
[56] G. Lin, W. He, and T. Van Nguyen, *Modeling liquid water effects in the gas diffusion and catalyst layers of the cathode of a PEM fuel cell*, J. Electrochem. Soc., 151 (2004), pp. A1999–A2006.
[57] S. Litster, C. R. Buie, T. Fabian, J. K. Eaton, and J. G. Santiago, *Active water management for PEM fuel cells*, J. Electrochem. Soc., 154 (2007), pp. B1049–B1058.
[58] S. Litster and N. Djilali, *Mathematical modelling of ambient air-breathing fuel cells for portable devices*, Electrochim. Acta, 52 (2007), pp. 3849–3862.
[59] C. Liu and J. Shen, *A phase field model for the mixture of two incompressible fluids and its approximation by a Fourier-spectral method*, Phys. D, 179 (2003), pp. 211–228.
[60] C. Liu and N. Walkington, *An Eulerian description of fluids containing visco-elastic particles*, Arch. Ration. Mech. Anal., 159 (2001), pp. 229–252.
[61] B. Markicevica, A. Bazylaka, and N. Djilali, *Determination of transport parameters for multiphase flow in porous gas diffusion electrodes using a capillary network model*, J. Power Sources, 171 (2007), pp. 706–717.
[62] N. M. Markovic, T. J. Schmidt, V. Stamenkovic, and P. N. Ross, *Oxygen reduction reaction on Pt and Pt bimetallic surfaces: A selective review*, Fuel Cells, 1 (2001), pp. 105–116.
[63] R. Matthias and R. Schatzle, *On a modified conjecture of De Giorgi*, Math. Z., 254 (2006), pp. 675–714.
[64] S. Mazumder and J. V. Cole, *Rigorous* 3*-D mathematical modeling of PEM fuel cells,* I. *Model predictions without liquid water transport*, J. Electrochem. Soc., 150 (2003), pp. A1503–A1509.
[65] S. Mazumder and J. V. Cole, *Rigorous* 3*-D mathematical modeling of PEM fuel cells,* II. *Model predictions with liquid water transport*, J. Electrochem. Soc., 150 (2003), pp. A1510–A1517.
[66] G. F. McLean, T. Niet, S. Prince-Richard, and N. Djilali, *An assessment of alkaline fuel cell technology*, Int. J. Hydrogen Energy, 27 (2002), pp. 507–526.
[67] J. P. Meyers and R. M. Darling, *Model of carbon corrosion in PEM fuel cells*, J. Electrochem. Soc., 153 (2006), pp. A1432–A1442.
[68] E. Middleman, *Improved PEM fuel cell electrodes by controlled self-assembly*, Fuel Cells Bull., No. 11 (2002), pp. 9–12.
[69] D. Natarajan and T. Van Nguyen, *A two-dimensional, two-phase, multicomponent, transient model for the cathode of a proton exchange membrane fuel cell using conventional gas distributors*, J. Electrochem. Soc., 148 (2001), pp. A1324–A1335.
[70] D. Natarajan and T. Van Nguyen, *Three-dimensional effects of liquid water flooding in the cathode of a PEM fuel cell*, J. Power Sources, 115 (2003), pp. 66–80.
[71] I. Nazarov and K. Promislow, *The impact of membrane constraint on PEM fuel cell water management*, J. Electrochem. Soc., 154 (2007), pp. B623–B630.
[72] V. Neburchilov, J. Martin, H. Wang, and J. Zhang, *A review of polymer electrolyte membranes for direct methanol fuel cells*, J. Power Sources, 169 (2007), pp. 221–238.
[73] S. Nemit-Nasser, *Micromechanics of actuation of ionic polymer-metal composites*, J. Appl. Phys., 92 (2002), pp. 2899–2915.

[74] P. T. Nguyen, T. Berning, and N. Djilali, *Computational model of a PEM fuel cell with serpentine gas flow channels*, J. Power Sources, 130 (2004), pp. 149–157.
[75] L. M. Onishi, J. M. Prausnitz, and J. Newman, *Water-Nafion equilibria. Absence of Schroeder's paradox*, J. Phys. Chem. B, 111 (2007), pp. 10166–10173.
[76] S. J. Paddison, *Proton conduction mechanisms in polymer electrolyte membranes at low degrees of hydration*, Ann. Rev. Mater. Res., 33 (2003), pp. 289–319.
[77] S. J. Paddison and J. A. Elliott, *Molecular modeling of the "short-side-chain" perfluorosulfonic acid membrane*, J. Phys. Chem. A, 109 (2005), pp. 7583–7593.
[78] S. J. Paddison and J. A. Elliott, *On the consequences of side chain flexibility and backbone conformation on hydration and proton dissociation in perfluorosulfonic acid membranes*, Phys. Chem. Chem. Phys., 8 (2006), pp. 2193–2203.
[79] U. Pasaogullari and C. Y. Wang, *Liquid water transport in gas diffusion layer of polymer electrolyte fuel cells*, J. Electrochem. Soc., 151 (2004), pp. A399–A406.
[80] R. Paul and S. J. Paddison, *The phenomena of dielectric saturation in the water domains of polymer electrolyte membranes*, Solid State Ionics, 168 (2004), pp. 245–248.
[81] R. Paul and S. J. Paddison, *Structure and dielectric saturation of water in hydrated polymer electrolyte membranes: Inclusion of the internal field energy*, J. Phys. Chem. B, 108 (2004), pp. 13231–13241.
[82] R. Paul and S. J. Paddison, *Effects of dielectric saturation and ionic screening on the proton self-diffusion coefficients in perfluorosulfonic acid membranes*, J. Chem. Phys., 123 (2005), p. 224704.
[83] R. L. Pego, *Front migration in the nonlinear Cahn-Hilliard equation*, Proc. Roy. Soc. London Ser. A, 422 (1989), pp. 261–278.
[84] L. Pisani, M. Valentini, and G. Murgia, *Analytical pore scale modeling of the reactive regions of polymer electrolyte fuel cells*, J. Electrochem. Soc., 150 (2003), pp. A1549–A1559.
[85] K. Promislow, P. Chang, H. Haas, and B. Wetton, *A two-phase unit cell model for slow transients in polymer electrolyte membrane fuel cells*, J. Electrochem. Soc., 155 (2008), pp. A494–A504.
[86] K. Promislow, J. Stockie, and B. Wetton, *A sharp interface reduction for multiphase transport in a porous fuel cell electrode*, Proc. R. Soc. Ser. Lond. Ser. A Math. Phys. Eng. Sci., 462 (2006), pp. 789–816.
[87] K. Promislow and B. Wetton, *A simple, mathematical model of thermal coupling in fuel cell stacks*, J. Power Sources, 150 (2005), pp. 129–135.
[88] K. Promislow and H. Zhang, *Global minimizers of functionalized Lagrangians*, submitted.
[89] C. A. Reiser, L. Bregoli, and T. W. Patterson, *A reverse-current decay mechanism for fuel cells*, Electrochem. Solid-State Lett., 8 (2005), pp. A273–A276.
[90] L. Rubatat, G. Gebel, and O. Diat, *Fibrillar structure of Nafion: Matching Fourier and real space studies of corresponding films and solutions*, Macromolecules, 37 (2004), pp. 7772–7783.
[91] B. Sakintunaa, F. Lamari-Darkrimb, and M. Hirscherc, *Metal hydride materials for solid hydrogen storage: A review*, Int. J. Hydrogen Energy, 32 (2007), pp. 1121–1140.
[92] S. Satyapal, J. Petrovic, C. Read, G. Thomas, and G. Ordaz, *The U.S. Department of Energy's National Hydrogen Storage Project: Progress towards meeting hydrogen-powered vehicle requirements*, Catalysis Today, 120 (2007), pp. 246–256.
[93] V. P. Schulz, J. Becker, A. Wiegmann, P. P. Mukherjee, and C.-Y. Wang, *Modeling of two-phase behavior in the gas diffusion medium of PEFCs via full morphology approach*, J. Electrochem. Soc., 154 (2007), pp. B419–B426.
[94] A. Shah, G. S. Kim, W. Gervais, A. Young, K. Promislow, J. Li, and S. Ye, *The effects of water and microstructure on the performance of polymer electrolyte fuel cells*, J. Power Sources, 160 (2006), pp. 1251–1268.
[95] M. Shahinpoor and K. Kim, *Ionic polymer-metal composites*: III. *Modeling and simulation as biomimetic sensors, actuators, transducers, and artificial muscles*, Smart Mater. Struct., 13 (2004), pp. 1362–1388.
[96] Y. D. Shikhmurzaev, *Moving contact lines in liquid/liquid/solid systems*, J. Fluid Mech., 334 (1997), pp. 211–249.
[97] N. P. Siegel, M. W. Ellis, D. J. Nelson, and M. R. von Spakovsky, *Single domain PEMFC model based on agglomerate catalyst geometry*, J. Power Sources, 115 (2003), pp. 81–89.
[98] N. P. Siegel, M. W. Ellis, D. J. Nelson, and M. R. von Spakovsky, *A two-dimensional computational model of PEMFC with liquid water transport*, J. Power Sources, 128 (2004), pp. 173–184.
[99] D. Song, Q. Wang, Z. Liu, T. Navessin, M. Eikerling, and S. Holdcroft, *Numerical optimization study of the catalyst layer of a PEM fuel cell cathode*, J. Power Sources, 126 (2004), pp. 104–111.

[100] D. Spernjaka, A. K. Prasada, and S. G. Advani, *Experimental investigation of liquid water formation and transport in a transparent single-serpentine PEM fuel cell*, J. Power Sources, 170 (2007), pp. 334–344.
[101] C. Spitta, J. Mathiak, M. Dokupil, and A. Heinzel, *Coupling of a small scale hydrogen generator and a PEM fuel cell*, Fuel Cells, 7 (2007), pp. 197–203.
[102] J. M. Stockie, K. Promislow, and B. R. Wetton, *A finite volume method for multicomponent gas transport in a porous fuel cell electrode*, Internat. J. Numer. Methods Fluids, 41 (2003), pp. 577–599.
[103] J. Stumper, H. Haas, and A. Granados, *In situ determination of MEA resistance and electrode diffusivity of a fuel cell*, J. Electrochem. Soc., 152 (2005), pp. A837–A844.
[104] W. Sun, B. A. Peppley, and K. Karan, *An improved two-dimensional agglomerate cathode model to study the influence of catalyst layer structural parameters*, Electrochim. Acta, 50 (2005), pp. 3359–3374.
[105] N. Vasileiadis, D. J. L. Brett, V. Vesovic, A. R. Kucernak, E. Fontes, and N. P. Brandon, *Numerical modeling of a single channel polymer electrolyte fuel cell*, J. Fuel Cell Sci. Tech., 4 (2007), pp. 336–344.
[106] C.-Y. Wang and C. Beckermann, *A two-phase mixture model of liquid-gas flow and heat transfer in capillary porous media,* I: *Formulation*, Int. J. Heat Mass Transf., 36 (1993), pp. 2747–2758.
[107] Q. Wang, M. Eikerling, D. Song, and Z. Liu, *Structure and performance of different types of agglomerates in cathode catalyst layer of PEM fuel cells*, J. Electroanal. Chem., 573 (2004), pp. 61–79.
[108] Z. H. Wang, C.-Y. Wang, and K. S. Chen, *Two-phase flow and transport in the air cathode of proton exchange membrane fuel cells*, J. Power Sources, 94 (2001), pp. 40–50.
[109] A. Weber and J. Newman, *Transport in polymer-electrolyte membranes.* III. *Model validation in a simple fuel-cell model*, J. Electrochem. Soc., 151 (2004), pp. A316–A339.
[110] A. Weber and J. Newman, *A theoretical study of membrane constraint in polymer-electrolyte fuel cells*, AIChE J., 50 (2004), pp. 3215–3226.
[111] A. Z. Weber and R. M. Darling, *Understanding porous water-transport plates in polymer-electrolyte fuel cells*, J. Power Sources, 168 (2007), pp. 191–199.
[112] A. Z. Weber, R. M. Darling, and J. Newman, *Modeling two-phase behavior in PEFCs*, J. Electrochem. Soc., 151 (2004), pp. A1715–A1727.
[113] A. Z. Weber and J. Newman, *Modeling transport in polymer-electrolyte fuel cells*, Chem. Rev., 104 (2004), pp. 4679–4726.
[114] A. Z. Weber and J. Newman, *Macroscopic modeling of polymer-electrolyte membranes*, in Advances in Fuel Cells, Elsevier, New York, 2007, pp. 47–117.
[115] J.-H. Wee and K.-Y. Lee, *Overview of the effects of rare-earth elements used as additive materials in molten carbonate fuel cell systems*, J. Mater. Sci., 41 (2006), pp. 3585–3592.
[116] H. Weng and C.-Y. Wang, *Model of two-phase flow and flooding dynamics in polymer electrolyte fuel cells*, J. Electrochem. Soc., 152 (2005), pp. A1733–A1741.
[117] J. Wescott, Y. Qi, L. Subramanian, and T. Capehart, *Mesoscale simulation of morphology in hydrated perfluorosulfonic acid membranes*, J. Chem. Phys., 124 (2006), 134702.
[118] B. Wetton, G.-S. Kim, K. Promislow, and K. St-Pierre, *PEM unit cell model considering additional reactions*, FUELCELL2006-97027, in Proceedings of the Fourth International Conference on Fuel Cell Science, Engineering and Technology, Irvine, CA, 2006; available online at http://www.asme.org.
[119] D. L. Wood, J. S. Yi, and T. V. Nguyen, *Effect of direct liquid water injection and interdigitated flow field on the performance of proton exchange membrane fuel cells*, Electrochim. Acta, 43 (1998), pp. 3795–3809.
[120] J. Xie, D. L. Wood, K. L. More, P. Atanassov, and R. L. Borup, *Microstructural changes of membrane electrode assemblies during PEFC durability testing at high humidity conditions*, J. Electrochem. Soc., 152 (2005), pp. A1011–A1020.
[121] J. Xie, D. L. Wood, K. L. More, P. Atanassov, and R. L. Borup, *Durability of PEFCs at high humidity conditions*, J. Electrochem. Soc., 152 (2005), pp. A104–A113.
[122] K. Yasuda, A. Taniguchi, T. Akita, T. Ioroi, and Z. Siroma, *Platinum dissolution and deposition in the polymer electrolyte membrane of a PEM fuel cell as studied by potential cycling*, Phys. Chem. Chem. Phys., 8 (2006), pp. 746–752.
[123] J. S. Yi and T. V. Nguyen, *An along-the-channel model for proton exchange membrane fuel cells*, J. Electrochem. Soc., 145 (1998), pp. 1149–1159.
[124] Z. H. Zhang, A. E. Marble, B. MacMillian, K. Promislow, J. Martin, H. Wang, and B. J. Balcom, *Spatial and temporal mapping of water content across Nafion membranes under wetting and drying conditions*, J. Magn. Reson., 194 (2008), pp. 245–253.